

**FRONTAL PASSAGE AND COLD POOL DETECTION
USING OKLAHOMA MESONET OBSERVATIONS**

by

Andrew T. Lesage

A thesis submitted to the faculty of
The University of Utah
in partial fulfillment of the requirements for the degree of

Master of Science

Atmospheric Sciences
The University of Utah

December 2012

Copyright © Andrew T. Lesage 2012

All Rights Reserved

THE UNIVERSITY OF UTAH GRADUATE SCHOOL

STATEMENT OF THESIS APPROVAL

The thesis of Andrew T. Lesage
has been approved by the following supervisory committee members:

First M. Last , Chair enter date

Date Approved

First M. Last , Member

Date Approved

First M. Last , Member

Date Approved

ABSTRACT

For over a dozen years the Oklahoma Mesonet network has provided surface observations at over 100 stations. These observations are used to analyze mass fluxes, frontal passages, and cold pools. Case studies are detailed and a 15-year climatology of frontal passages and cold pools was computed in this research.

Updrafts, downdrafts, and precipitation are most strongly correlated in the summer months and least correlated in the winter months. Wet spring and summer days had the highest average convergence and divergence values while dry summer and fall days had the lowest average convergence and divergence.

Frontal passages and cold pools are tracked throughout the Mesonet in various case studies, four of which are covered herein. Those cases are 1) 13 June 1997, 2) 15-16 June 2002, 3) 20 May 2011, and 4) 24-25 May 2011. The methodology is able to represent front location and cold pool areas quite well despite the low resolution of the Mesonet grid.

The climatology of front and cold pool data yielded many similarities. Winter has the largest magnitude changes in ΔT , ΔP , and $\Delta h/cp$ while spring and fall had the largest magnitude change in Δq_v . Summer has the lowest with the exception of spring ΔT . Correlations between these variables are lowest in the more convectively active summer season. Convergence is roughly equal ahead of fronts from spring through fall; however, divergence is present in summer frontal passages earlier and stronger compared to the other seasons. Fronts and cold pools are most likely to occur in summer and spring with summer having the highest percentage of fronts which lead to cold pools. Fronts and cold pools are substantially more likely to occur during the late afternoon and early evening in the summer; other seasons had a slighter nocturnal increase in frequency. Western Oklahoma had higher frequencies of frontal passages and cold pools than Eastern Oklahoma with frontal passages having the

stronger signal.

These findings help identify seasonal, diurnal, and geographic distributions of fronts and cold pools and can be used in modeling studies to better the understanding of cold pool processes and parameterizations.

CONTENTS

ABSTRACT	iii
LIST OF FIGURES	vii
LIST OF TABLES	xi
ACKNOWLEDGMENTS	xii
CHAPTERS	
1. INTRODUCTION AND LITERATURE REVIEW	1
1.1 Defining a Convective Cold Pool	1
1.2 Outflow Boundaries	2
1.3 Squall Line and Bow Echo Studies	3
1.4 MCS Studies	4
1.5 Parameterization Studies	5
1.5.1 Shallow and Deep Convection	5
1.5.2 Other Parameterizations	5
2. DATA	8
2.1 Oklahoma Mesonet	8
2.2 Arkansas-Red Basin River Forecast Center Gridded Precipitation	9
3. METHODOLOGY	11
3.1 Mass Flux Estimates	11
3.2 Precipitation	12
3.3 Frontal Analysis	12
3.4 Cold Pool Analysis	17
4. RESULTS: MASS FLUXES AND PRECIPITATION	18
4.1 Mass Fluxes	18
4.2 Precipitation	18
5. RESULTS: CASE STUDIES	23
5.1 13 June 1997 Case	23
5.2 15-16 June 2002 Case	26
5.3 20 May 2011 Case	30
5.4 24-25 May 2011 Case	34

6. RESULTS: 15-YEAR CLIMATOLOGY OF FRONTS AND COLD POOLS	39
6.1 Variable Changes (T , P , q_v , and h_{cp}^{-1})	39
6.2 Convergence/Divergence	41
6.3 Seasonal Distribution	43
6.4 Diurnal Distribution	44
6.5 Geographic Distribution	47
7. DISCUSSION	55
7.1 Research Findings	55
7.2 Comparisons to Previous Studies	56
8. CONCLUSIONS	58
8.1 Summary of Results	58
8.2 Future Research Possibilities	60
REFERENCES	61

LIST OF FIGURES

2.1 Map of the Oklahoma Mesonet grid used for 1997. Delaunay triangulation was used to plot the stations onto the grid and particularly long and skinny triangles were removed. Removed triangles were primarily on the outer border with the exception of two near 98W and 35N.	10
3.1 Hourly precipitation total ending at 8z on 2 May 1997 in mm/hr from (a) ABRFC radar estimated precipitation and (b) Oklahoma Mesonet precipitation observations. The box indicates the area used to determine the ABRFC total Mesonet precipitation estimate. Only the area inside the triangles is considered for the Oklahoma Mesonet total precipitation estimate.	13
3.2 Front scores for the JJA 1997 period at the Blackwell Mesonet station (36.75N, 97.25W). High, positive front scores indicate frontal passages.	16
4.1 Oklahoma Mesonet monthly values for M_u (green), M_d (cyan), M_u^+ (red), and M_d^+ (blue) over the 1997-2011 period. These values are averaged over the entire Mesonet area. Since stronger divergence/convergence is a subset of all convergence/divergence M_u^+ and M_d^+ are higher in magnitude than M_u and M_d	19
4.2 Annual cycle of (a) M_d , (b) M_d^+ , (c) M_u , and (d) M_u^+ values for the Oklahoma Mesonet with the average and range plotted. Divergence and convergence are stronger on average in spring than the other seasons while convergence is weakest in September and divergence weakest in November/December.	20
4.3 Oklahoma Mesonet (a) monthly average precipitation values over the 1997-2011 period and (b) the monthly averages and range of the annual cycle of precipitation.	21
4.4 Seasonal average and 1stdev. for (a) M_u^+ and (b) M_d^+ for wet (Mesonet area averaged precip. > 1mm) and dry (0 precip.) days. Wet spring and summer days have the strongest average updrafts and downdrafts while dry summer days have the weakest.	22

5.1	Front analysis for 13 June 1997 (a) 0300 UTC, (b) 0500 UTC, (c) 0700 UTC, and (d) 0900 UTC. Red dots are convergence $> 10^{-4}s^{-1}$ while blue dots are divergence $\geq 10^{-4}s^{-1}$. Yellow lines are fronts where the three corners of the triangle have FSs of 3+ during frontal passage while magenta lines are fronts where the triangle corners have FSs are 5+. White squares are stations where at the current timestep the FS is $3 \leq FS < 5$; black squares designate stations currently with FSs at 5+. Radar images are from the UCAR image archive.	24
5.2	Cold pool analysis for 13 June 1997 (a) 0330 UTC, (b) 0500 UTC, (c) 0700 UTC, and (d) 0900 UTC. Black dots mark triangles that are in cold pools at this time. Fronts from Figure 5.1 are shown for context. Radar images are from the UCAR image archive.	25
5.3	Cold pool areas for the 13 June 1997 0-12 UTC case study. Cold pool areas are shown for total area in cold pools (blue), area that becomes part of a cold pool the given timestep (green), area that has been in a cold pool at least 30 minutes (purple), and area that has been in a cold pool at least 60 minutes (black).	27
5.4	Front analysis for 16 June 2002 (a) 0000 UTC, (b) 0130 UTC, (c) 0300 UTC, and (d) 0430 UTC. Red dots are convergence $> 10^{-4}s^{-1}$ while blue dots are divergence $\geq 10^{-4}s^{-1}$. Yellow lines are fronts where the three corners of the triangle have FSs of 3+ during frontal passage while magenta lines are fronts where the triangle corners have FSs are 5+. White squares are stations where at the current timestep the FS is $3 \leq FS < 5$; black squares designate stations currently with FSs at 5+. Radar images are from the UCAR image archive.	28
5.5	Cold pool analysis for 16 June 2002 (a) 0000 UTC, (b) 0130 UTC, (c) 0300 UTC, and (d) 0430 UTC. Black dots mark triangles that are in cold pools at this time. Fronts from Figure 5.4 are shown for context. Radar images are from the UCAR image archive.	29
5.6	Same as Figure 5.3, except for the 15-16 June 2002 20-8 UTC case study.	31
5.7	Front analysis for 20 May 2011 (a) 0900 UTC, (b) 1100 UTC, (c) 1300 UTC, and (d) 1500 UTC. Red dots are convergence $> 10^{-4}s^{-1}$ while blue dots are divergence $\geq 10^{-4}s^{-1}$. Yellow lines are fronts where the three corners of the triangle have FSs of 3+ during frontal passage while magenta lines are fronts where the triangle corners have FSs are 5+. White squares are stations where at the current timestep the FS is $3 \leq FS < 5$; black squares designate stations currently with FSs at 5+. Radar images are from the UCAR image archive, NEXLAB - College of DuPage.	32
5.8	Cold pool analysis for 20 May 2011 (a) 0900 UTC, (b) 1100 UTC, (c) 1300 UTC, and (d) 1500 UTC. Black dots mark triangles that are in cold pools at this time. Fronts from Figure 5.7 are shown for context. Radar images are from the UCAR image archive.	33
5.9	Same as Figure 5.3, except for the 20 May 2011 8-20 UTC case study. .	35

5.10	Front analysis for 24 May 2011 (a) 2000 UTC, (b) 2200 UTC, 25 May 2011 (c) 0000 UTC, and (d) 0200 UTC. Red dots are convergence $> 10^{-4}s^{-1}$ while blue dots are divergence $\geq 10^{-4}s^{-1}$. Yellow lines are fronts where the three corners of the triangle have FSs of 3+ during frontal passage while magenta lines are fronts where the triangle corners have FSs are 5+. White squares are stations where at the current timestep the FS is $3 \leq FS < 5$; black squares designate stations currently with FSs at 5+. Radar images are from the UCAR image archive, NEXLAB - College of DuPage.	36
5.11	Cold pool analysis for 24 May 2011 (a) 2000 UTC, (b) 2200 UTC, 25 May 2011 (c) 0000 UTC, and (d) 0200 UTC. Black dots mark triangles that are in cold pools at this time. Fronts from Figure 5.10 are shown for context. Radar images are from the UCAR image archive.	37
5.12	Same as Figure 5.3, except for the 24-25 May 2011 18-6 UTC case study.	38
6.1	Seasonally averaged diurnal cycle (in UTC time) of all frontal passages at triangles in the Oklahoma Mesonet from the 1997-2011 period along with standard deviations. Results are shown for (a) spring, (b) summer, (c), fall, and (d) winter and for all frontal passages (red) and strong frontal passages (blue).	46
6.2	Seasonally averaged diurnal cycle (in UTC time) of all cold pools at triangles in the Oklahoma Mesonet from the 1997-2011 period along with standard deviations. Results are shown for (a) spring, (b) summer, (c), fall, and (d) winter and for all frontal passages which yielded cold pools (red) and strong frontal passages which yielded cold pools (blue).	47
6.3	Seasonally averaged diurnal cycle (in UTC time) of the percentage of all (red) and strong (blue) fronts that yield cold pools. Results are shown for (a) spring, (b) summer, (c), fall, and (d) winter.	48
6.4	Scatterplots with linear regression lines for (a) annually averaged frontal passage frequency and Mesonet triangle area, (b) annually averaged strong frontal passage frequency and Mesonet triangle area, (c) annually averaged frontal passage frequency and longest Mesonet triangle side length, and (d) annually averaged strong frontal passage frequency and longest Mesonet triangle side length.	49
6.5	Scatterplots with linear regression lines for (a) annually averaged cold pool frequency and Mesonet triangle area, (b) annually averaged strong cold pool frequency and Mesonet triangle area, (c) annually averaged cold pool frequency and longest Mesonet triangle side length, and (d) annually averaged strong cold pool frequency and longest Mesonet triangle side length.	50

6.6	Geographic distribution of (a) all frontal passages, adjusted for triangle area, (b) strong frontal passages, adjusted for triangle area, (c) all frontal passages, adjusted for maximum triangle side length, and (d) strong frontal passages, adjusted for maximum triangle side length. Size of dots represents the number of years the triangle centroid was at that location (1997-2011). Only triangles that were present more than 5 years are shown. The grid is the 1997 triangles; since the grid can change each year the 1997 grid is only a close representation.	52
6.7	Geographic distribution of (a) all fronts which yield cold pools, adjusted for triangle area, (b) strong fronts which yield cold pools, adjusted for triangle area, (c) all fronts which yield cold pools, adjusted for maximum triangle side length, and (d) strong fronts which yield cold pools, adjusted for maximum triangle side length. Size of dots represents the number of years the triangle centroid was at that location (1997-2011). Only triangles that were present more than 5 years are shown. The grid is the 1997 triangles; since the grid can change each year the 1997 grid is only a close representation.	53

LIST OF TABLES

4.1	Correlation table for each of the 4 seasons using the 15-yr of Mesonet observations for M_u , M_d , M_u^+ , M_d^+ , and precipitation (Prec).	20
6.1	Average ΔT , ΔP , Δq_v , and Δhcp^{-1} for all frontal passage (FS3+ / FS5+).	40
6.2	Average ΔT , ΔP , Δq_v , and Δhcp^{-1} during frontal passages that yield cold pools (FS3+ / FS5+).	40
6.3	Correlations between ΔT , ΔP , Δq_v , and Δhcp^{-1} for all frontal passages (FS3+ / FS5+).	42
6.4	Correlations between ΔT , ΔP , Δq_v , and Δhcp^{-1} for frontal passages which yield cold pools (FS3+ / FS5+).	42
6.5	Divergence values at the beginning, middle, and end of all triangle frontal passages experienced by Mesonet triangles from 1997-2011 by season (FS3+ / FS5+) in s^{-1}	44
6.6	Divergence values at the beginning, middle, and end of triangle frontal passages yielding cold pools experienced by Mesonet triangles from 1997-2011 by season (FS3+ / FS5+) in s^{-1}	44
6.7	Number of frontal passages and cold pools experienced by Mesonet triangles from 1997-2011 by season (FS3+ / FS5+).	45
6.8	Average magnitude of Student t -scores from distribution of difference between mean scores for triangles that were present in the Mesonet for over 5 years. Values are given for fronts and cold pools of both strengths. The Original column contains the t -scores for the original grid. The Grid column refers to t -scores for the grid adjusted to remove triangles with too-large side lengths. The final two columns have the t -scores with the grid adjustment and the area and triangle side length adjustments, respectively.	54

ACKNOWLEDGMENTS

This research was supported by the Office of Science (BER), U.S. Department of Energy, Grant No. DE-FG02-08ER64553.

Data were obtained from the Atmospheric Radiation Measurement (ARM) Program sponsored by the U.S. Department of Energy, Office of Science, Office of Biological and Environmental Research, Climate and Environmental Sciences Division. Gridded precipitation data was obtained from the National Weather Service Arkansas-Red Basin River Forecast Center. Radar images are from the University Corporation for Atmospheric Research (UCAR) image archive.

I would like to thank my committee members, Professor Edward Zipser, Dr. Zhaoxia Pu and particularly my advisor Professor Steven Krueger for providing the opportunity to study and work on research at the University of Utah.

Finally I would like to thank my family and friends for their love and support.

CHAPTER 1

INTRODUCTION AND LITERATURE REVIEW

Cold pools are a prominent and common feature of convective storms though are less studied than other convective features. This research seeks to identify cold pools in surface observations retrieved from the Oklahoma Mesonet. First, however, it is necessary to define a convective cold pool. Sections will follow on various types of studies on convective systems and features that influence or are influenced by cold pools: outflow boundaries, squall lines and bow echoes, and mesoscale convective systems (MCSs). Finally, a section on studies focused on parameterizations related to cold pools and related to convective processes concludes this chapter.

1.1 Defining a Convective Cold Pool

Convective cold pools have been studied for over half a century. Observations from the Thunderstorm Project showed evaporative cooling leading to descent in the region behind a squall line (Newton, 1950). A convergence/divergence pattern was also noted as a prominent feature in case studies of these squall lines. The results were similar to that observed by (Tepper, 1950) near Wilmington, Ohio where pressure jumps, temperature falls, wind, and precipitation features were observed with squall lines. Tepper referred to the squall lines as propagated "pressure jump lines".

Fujita further developed the description of the pressure fields present in squall lines. In his synoptic analysis of squall lines in the Central United States, Fujita identified three main features of a pressure field: the pressure surge line, the thunderstorm high, and the wake depression (Fujita, 1955). The pressure surge line marks the leading edge of the thunderstorm and moves in the direction the storm will propagate. The thunderstorm high, which later would be more commonly known as

a mesohigh, is the high pressure region led by the pressure surge line and contains cool downdrafts that spread out upon reaching the surface. The region of surface cooling from these downdrafts is what would become known as the cold pool of the thunderstorm and is often associated with the mesohigh. The wake depression is a region of low pressure oftentimes behind the thunderstorm high that forms a pressure dipole with the thunderstorm high.

Based on this early work, a convective cold pool is a region of cold air at the surface produced by downdrafts in a convectively initiated system. The cooling is heavily influenced by evaporative precipitation. A pressure jump is expected as well as surface divergence resulting from downdrafts reaching the surface.

1.2 Outflow Boundaries

One of the important features of a convective cell is the outflow characteristics. Outflow boundaries can mark the edge of a cold pool as subsiding air reaching the surface spreads out.

Modeling of the outflow and the convection of a storm is crucial to accurate representation of the storm evolution. These outflows oftentimes feed back into the convective region of the thunderstorm, allowing the storm to maintain intensity, or form new convective cells as has been found in cloud model simulations (Wilhelmson and Klemp, 1978). Simulations have found that cells can continue to develop for hours at roughly half hour intervals along the progressing outflow boundary (Wilhelmson and Chen, 1982). Downdraft development was the primary source of the largest near-surface changes in the study.

It has also been found that outflows from multiple clouds can induce lifting, warming, and moistening where they collide (Droegemeier and Wilhelmson, 1985a). In that study, the outflow from two initial clouds triggered a pair of clouds to form with the upshear cloud continuing to grow. The downdrafts of the upshear cloud prevented further development of the downshear cloud. A third cloud formed from the air lifted over the gust front. A model simulation was run and found that vertical wind shear strength was the primary factor in determining the growth of the upshear and downshear clouds with weaker wind shear allowing for both to grow

(Droegemeier and Wilhelmson, 1985b). Further research on thunderstorm outflows examined parameters related to cold air sources (Droegemeier and Wilhelmson, 1987). These cold air sources are the vertical temperature profile, the magnitude of the temperature deficit, and the cold-air depth. The vertical temperature profile was the primary controlling factor of the three due to its influence on the gust front speed and outflow depth.

Outflow boundaries can interact with other boundary layers such as drylines. In a case study during the Verification of the Origins of Rotation in Tornadoes Experiment (VORTEX) it was found that a residual dryline secondary circulation (RDSC) formed above the cold pool (Weiss and Bluestein, 2002). Proposed methods of convective initiation in the particular case were superposition of boundaries and the possibility of the outflow boundary causing parcels to reach their LCL west of the dryline.

1.3 Squall Line and Bow Echo Studies

Various studies have looked at the sustainability of squall lines with or without cold pools. One such study found that the interaction of a storm's surface cold pool outflow with low-level shear leads to deeper and less inhibited lifting which allows for new cells to form more easily (Rotunno et al., 1988). However, it has also been found that a squall line can sustain itself even without a cold pool present, as was the case in a cast study using the fifth-generation Pennsylvania State University-NCAR Mesoscale Model (MM5) (Stoelinga et al., 2003). In the case without a cold pool, a cold front aloft provided the main source of lifting to sustain the squall line.

A cloud-resolving model at high-resolution has been used to study tropical deep convection generated cold pools (Tompkins, 2001). Tompkins had found an average lifetime of 2.5 h and an average maximum radii of 8.6 km. From the study a three stage model was developed. Stage one involves cooling and moistening through evaporated air below the area of convection. Stage two involves the spreading of a boundary layer cold pool. The final stage involves the entrainment of elevated air into the weakening downdraft. This study also found that cold pools are initiated in low wind shear cases predominantly due to thermodynamical causes rather than dynamical causes.

Cold pool features accompany bow echoes as well. Using model simulations of

bow echoes it was found that long-lived bowing segments develop most favorably with intermediate strengths of cold pools where strength is considered in terms of moisture content (James et al., 2006). Cold pools that were too strong tended to lose heterogeneity in structure before a bow can develop in the line.

Oklahoma Mesonet data has been used to find dozens of bow echo cases (Adams-Selin and Johnson, 2010). Adams-Selin and Johnson produced a conceptual model for the stages for bow echoes in this study which is composed of four stages: 1) initial formation of the convective line, 2) the pressure surge, 3) new bowing, and 4) dissipation. These cases contain the characteristic pressure rise and temperature drop associated with cold pools.

1.4 MCS Studies

Many observational studies of mesoscale convective systems (MCSs) have allowed for analysis of cold pools.

There has been extensive study of various squall line and bow echo cases throughout the years. Pressure features and precipitation structure have been detailed in Oklahoma-Kansas Preliminary Regional Experiment for STORM-Central (OK PRE-STORM) case studies of squall lines and MCSs (Johnson and Hamilton, 1988; Stumpf and Johnson, 1991; Loehrer and Johnson, 1995).

In Johnson and Hamilton, the wake low life cycle was detailed in its close association just behind the stratiform components of precipitation. The cold pool is collocated with the mesohigh just behind the region of largest downdrafts from the convective line. The primary finding in Stumpf et al. was that trailing stratiform regions of MCSs resulted in warming of the lower troposphere, strong low-level winds, and a pressure gradient observed that is associated with a wake low. The Loehner and Johnson study found that, despite a large variety in initial structure of precipitation, storms tended to develop, through varying paths, to an asymmetrical pattern with leading convective lines with stronger cells to the south and trailing stratiform precipitation predominantly in the left rear flank.

Flow relative to cold pools and the conditional instability distribution along gust fronts were shown to be a primary determinant on the propagation direction of an MCS (Corfidi, 2003). Corfidi found that for many MCSs this direction coincides with

the direction of the low-level jet; however, for bow-echo systems where the system may move faster than the mean wind, the downwind vector is more representative of their motion.

A four stage convective life cycle for a mesoscale convective system (MCS) was developed from Oklahoma Mesonet data from cases resulting in cold pools: 1) first storms, 2) MCS initiation, 3) mature MCS, and 4) MCS dissipation (Engerer et al., 2008). A mean temperature decrease of 9.5K and a mean pressure increase of 4.5mb was found for the first storms life cycle stage with these magnitudes of change dropping slightly throughout the rest of the life cycle.

Cold pools are important to have represented accurately in severe weather forecasting. In one particular modeling case study, the model success was highly dependent on having a reasonably accurate initialization of low-level flow patterns allowing for improvements in model predictions of later cells (Romero et al., 2001).

1.5 Parameterization Studies

1.5.1 Shallow and Deep Convection

Parameterizations of deep convection have been proposed over the years with the mass flux scheme commonly used (Arakawa and Schubert, 1974). Arakawa and Schubert's method involves parameterizing cumulus convection through use of the vertical distribution of mass flux, the entrainment and detrainment rates, and thermodynamic properties. Their cloud work function is the resulting closed parameterization.

With schemes developed for shallow convection and deep convection, a necessary task undertaken in recent years is to develop a bridge to span between the two. One approach is through the use of evaporative precipitation (Hohenegger and Bretherton, 2011). Cloud base mass flux, cloud base humidity, and entrainment and detrainment rates were adjusted in the University of Washington shallow convection scheme to improve simulation of deep convection with the "bulk updraft lateral mixing rate" adjustment having the largest influence.

1.5.2 Other Parameterizations

An early attempt to parameterize variables related to cold pools was when Fujita developed a method for estimating the relationship between rain evaporation in a

convective system to the hydrostatic surface pressure anomaly in a cold pool (Fujita, 1959). It was found that the increased cold air mass and the evaporated rain had a quantitative relationship dependent on the temperature lapse rate below cloud base. As a result, pressure changes at the surface in connection in cold pools can lead to parameterized estimates of rain evaporation.

One of the issues models were running into in the 1990s was that ground networks and models were insufficient to initialize cold pools. A study of National Centers for Environmental Prediction (NCEP) mesoscale Eta model forecasts was performed (Stensrud et al., 1999) which initialized 1) parameterized convection, 2) planetary boundary layer and surface physics, 3) explicit microphysics, and 4) initialization and data assimilation. It was found that the model was significantly influenced by cold pools in model results for cases where the large scale forcing was rather weak and vice versa.

Recent research has looked at parameterizing processes related to cold pools. Available lifting energy (ALE) and available lifting power (ALP) were used in the ALE/ALP closure method created to represent the coupling between the convection and the cold pool (Grandpeix and Lafore, 2010). This closure scheme was able to more realistically represent moist convective processes and to simulate cases in a single column model with results close to the observations and cloud resolving model (CRM) simulations (Grandpeix et al., 2010).

Finally, bulk microphysics schemes for multi-moment models have been developed to enhance evaluation of the microphysics involved in cold pools relative to single-moment schemes (Dawson II et al., 2010). Several advantages in their scheme were improved representation of evaporation, drop size distributions, and reduction of the cold bias found in single-moment schemes when it came to representing a supercell outbreak.

The rest of this paper is organized as follows. The description of the Oklahoma Mesonet and precipitation data is detailed in Chapter 2. Mass flux, precipitation, frontal passage, and cold pool methodology is outlined in Chapter 3. Results for mass flux and precipitation data is covered in Section 4. Several case studies, covering 13 June 1997 and 20 May 2011 are detailed in Chapter 5. 15-year front and cold pool

climatologies are detailed in Chapter 6. This includes the changes in key variables during frontal passages, the convergence/divergence associated with frontal passages, and the seasonal, diurnal, and geographic distribution of frontal passages and cold pools. The discussion of the results is located in Chapter 7 while the conclusions and future work make up Chapter 8.

CHAPTER 2

DATA

2.1 Oklahoma Mesonet

The Department of Energy Atmospheric Radiation Measurement (ARM) Programs' Oklahoma Mesonet is the primary dataset used in this research (Brock et al., 1995; McPherson et al., 2007). The Oklahoma Mesonet is sponsored by the University of Oklahoma and Oklahoma State University. Data from the Mesonet have been collected since 1994 at a five minute frequency. Over 100 stations are distributed roughly 40 km apart with at least one station in each county of Oklahoma.

Stations have been added over the years but for the purposes of this study, only the initial 114 stations that were present in 1997 are considered. Six of these stations are located in the Oklahoma Panhandle and are excluded. For the remaining stations, each station is used in this study only for the years in which the focus variables all exceed the observation threshold of 90% of annual measurement times having data recorded. The focus variables used in this study are longitude, latitude, altitude, 1.5-m air temperature, 1.5-m relative humidity, 10-m vector average wind magnitude, 10-m vector average wind direction, station pressure, and surface precipitation. Longitude and latitude only change in the case of a few stations which changed location over the 15 year period (1997-2011). Those stations were excluded the year that they moved. Each year had between 99 and 104 of the 108 non-panhandle stations meet the observation threshold.

Mesonet stations that met the observation threshold for a year were interpolated using the Delaunay triangulation procedure (Fig. 2.1). The resulting grid contains some extremely narrow triangles along the border which have been removed. Two stations very close to each other located near 35N 98W resulted in two small, narrow triangles which have also been removed. Additionally, in the process of this study

it was determined that triangles with too long a side length were not representative so any triangle with a maximum side length of at least 80km was excluded. This resulted in the removal of 10-13 triangles each year. Due to the varying number of stations that met the observation threshold each year, the grid is adjusted slightly from year to year.

2.2 Arkansas-Red Basin River Forecast Center Gridded Precipitation

A 4 km x 4 km gridded precipitation dataset produced by the Arkansas-Red Basin River Forecast Center (ABRFC) was used in this study to compare to the Oklahoma Mesonet precipitation values. The ABRFC gridded precipitation values are a result of a combination of Weather Surveillance Radar 88 Doppler (WSR-88D) Next-Generation Radar (NEXRAD) (Crum et al., 1993, 1998) precipitation estimates and rain gauge reports (Fulton et al., 1998). The inclusion of rain gauge reports to help reduce radar estimate biases has made the gridded precipitation values reliable at monthly and daily timescales (Grassotti et al., 2003). These gridded precipitation estimates are available from 24 June 1994 though only the period from May-August 1997 was used in this study for the purposes of determining whether or not the Mesonet precipitation values are representative of the Oklahoma Mesonet domain.

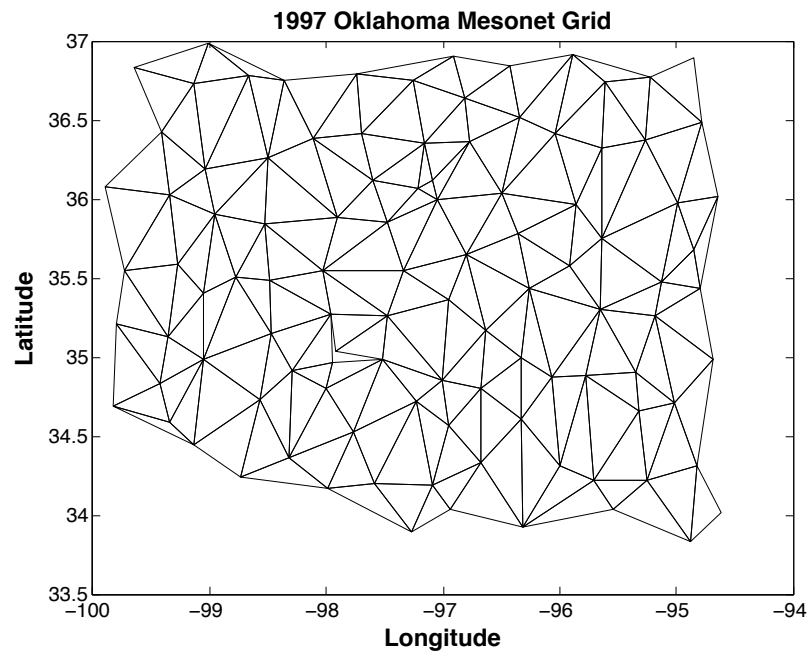


Figure 2.1 – Map of the Oklahoma Mesonet grid used for 1997. Delaunay triangulation was used to plot the stations onto the grid and particularly long and skinny triangles were removed. Removed triangles were primarily on the outer border with the exception of two near 98W and 35N.

CHAPTER 3

METHODOLOGY

3.1 Mass Flux Estimates

The procedure from Sun and Krueger (2012) was used to estimate the updraft and downdraft mass fluxes using estimates of surface divergence averaged over the Mesonet domain. Sun and Krueger's equations for surface convergence M_u (Eq. 3.1) and surface divergence M_d (Eq. 3.2) are

$$M_u = \frac{-\sum_i(A_i)div_iH(-div_i)}{\sum_i A_i} \quad (3.1)$$

$$M_d = \frac{\sum_i(A_i)div_iH(div_i)}{\sum_i A_i} \quad (3.2)$$

where div_i is the horizontal divergence of the i th triangle, A_i is the area of the i th triangle, and $H(x)$ is the Heaviside step function. Additionally, regions of strong convergence and divergence are identified to better identify likely regions of precipitation. M_u^+ and M_d^+ are identified as in Eq. 3.1-3.2 except the Heaviside step function only accepts regions of convergence or divergence that exceed a magnitude $> 10^{-4}s^{-1}$.

A set of determinants (Eq. 3.3-3.6) was used to calculate the divergence of triangles that are part of an irregular grid and has previously been applied to mesonet datasets (Davies-Jones, 1993; Dubois and Spencer, 2005).

$$a = \frac{\det \begin{pmatrix} u_2 - u_1 & y_2 - y_1 \\ u_3 - u_1 & y_3 - y_1 \end{pmatrix}}{2A(0)} \quad (3.3)$$

$$d = \frac{\det \begin{pmatrix} x_2 - x_1 & v_2 - v_1 \\ x_3 - x_1 & v_3 - v_1 \end{pmatrix}}{2A(0)} \quad (3.4)$$

$$A(0) = \frac{\det \begin{pmatrix} x_2 - x_1 & y_2 - y_1 \\ x_3 - x_1 & y_3 - y_1 \end{pmatrix}}{2} \quad (3.5)$$

$$\text{div} = a + d \quad (3.6)$$

3.2 Precipitation

Mesonet precipitation values were determined through an area-average over the entire Mesonet domain. The area-averaging was calculated by attributing each station precipitation observation to 1/3 of the area of each triangle in which the station was a corner. Since the Mesonet precipitation estimate over the domain uses only 100 points, a comparison with the ABRFC gridded precipitation values was performed to check the representativeness of the Mesonet precipitation data.

The ABRFC grid is defined as an average of all the points with longitudinal boundaries of 100W and 94.5W as well as latitudinal boundaries of 33.8N and 37.0N. A corner of the boundary that's entirely outside of Oklahoma is left out as well, stretching from 33.8N 97.6W to 34.6N 100W with points to the southwest dropped while points northeast were retained in the comparison. The ABRFC domain is the grid marked in magenta (Fig. 3.1a).

Hourly precipitation totals for the Oklahoma Mesonet and ABRFC datasets were generated for the May-August 1997 period. The correlation between the four months of hourly estimates of Mesonet precipitation, using these two methods, was 0.95. The strong correlation suggests that filling in the gaps in triangles using interpolation of the Mesonet station values is capable of adequately representing the precipitation totals derived from the ABRFC radar estimates. A case comparison of the two datasets for a 1hr period from 7-8z 2 May 1997 shows a strong likeness, largely a result of ABRFC data taking in surface rain gauge values including the Oklahoma Mesonet (Fig. 3.1).

3.3 Frontal Analysis

Identifying frontal passages in the Oklahoma Mesonet is necessary to identify convective cold pools. However, not all frontal passages have an associated cold pool.

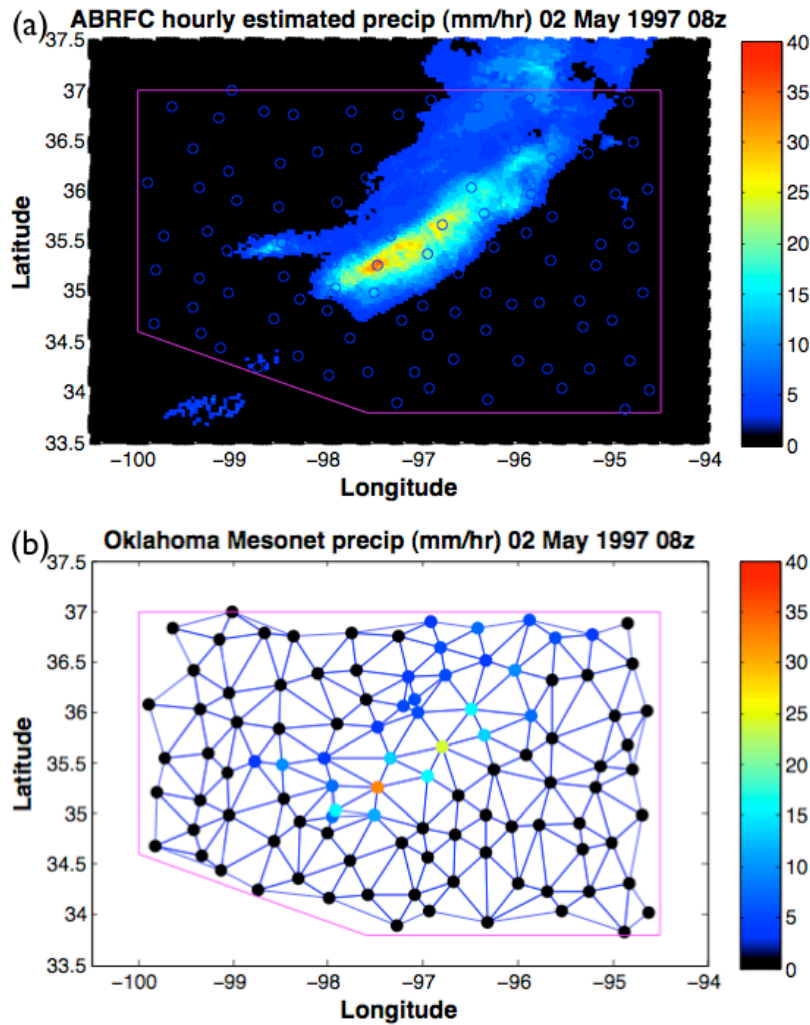


Figure 3.1 – Hourly precipitation total ending at 8z on 2 May 1997 in mm/hr from (a) ABRFC radar estimated precipitation and (b) Oklahoma Mesonet precipitation observations. The box indicates the area used to determine the ABRFC total Mesonet precipitation estimate. Only the area inside the triangles is considered for the Oklahoma Mesonet total precipitation estimate.

Cold pools are marked on the leading edge by a gust front. Previous studies have shown that temperature falls and pressure rises are associated with cold pools and these gust fronts (Engerer et al., 2008; Adams-Selin and Johnson, 2010).

Pressure and temperature values at each station were adjusted to account for the diurnal cycle. The diurnal cycle was calculated by averaging over the up to 15 years that a station was valid for at the same timestep (i.e. 0000z, 0005z, ..., 2355z) and then using five day averages centered on the day. For example, 12 June 0000z's diurnal

value at a station would be the average of all 0000z observations at that station from 10-14 June for the 15 year dataset. Similarly, the diurnal cycle was also removed for the pressure observations.

Pressure and temperature values at each station were also adjusted to account for the differences in elevation. Each station was adjusted to the Mesonet-averaged elevation, between 365 and 370m depending on year since only stations which met the observation threshold in a particular year were included in the average altitude for that year.

For pressure, the elevation adjustment involved several steps based on equations from Wallace and Hobbs (2006). Using temperature before diurnal adjustments were made, the saturation vapor pressure, e_s , is calculated (Eq. 3.7). Using saturation vapor pressure and relative humidity (RH), the vapor pressure (e), water vapor mixing ratio (q_v), virtual temperature (T_v), and then finally elevation adjusted pressure changes are calculated (Eq. 3.8-3.11). $T_0 = 273.15\text{K}$ while $Z_{station}$ and Z_{mean} are the altitudes of the Mesonet station and the mean of the Mesonet station altitudes. Since the diurnal and elevation changes are desired, the change in pressure with the elevation adjustment only is applied to the diurnal adjusted temperature (Eq. 3.12). The T used in the equations for e_s and T_v , however, are the observed temperatures before diurnal adjustment.

$$e_s = 6.11 * \exp^{[5420 * (\frac{1}{T_0} - \frac{1}{T})]} \quad (3.7)$$

$$e = e_s * \frac{RH}{100} \quad (3.8)$$

$$q_v = \frac{.622 * e}{P - e} \quad (3.9)$$

$$T_v = T * (1 + .61 * q_v) \quad (3.10)$$

$$P_{elev.} = P * \exp^{\frac{Z_{station} - Z_{mean}}{29.3 * T_v}} \quad (3.11)$$

$$P_{diur.,elev.} = P_{diur.} - (P - P_{elev.}) \quad (3.12)$$

For temperature, the elevation adjustment was calculated by lifting or lowering the station value dry adiabatically to the average elevation using Eq. 3.13.

$$T_{diur.,elev.} = T_{diur.} + 9.8 * (Z_{mean} - Z_{station})/1000 \quad (3.13)$$

Additionally, the change in moist static energy (dh/cp) was calculated in temperature units (K) using the elevation adjusted temperatures and water vapor mixing ratio (Eq. 3.14)

$$dh/cp = T_{final,diur.,elev.} - T_{initial,diur.,elev.} + L/c_p * (q_{v,final} - q_{v,initial}) \quad (3.14)$$

where L is the latent heat of evaporation, 2.5×10^6 J/kg, and c_p is the specific heat of dry air at constant pressure, 1004 J/kgK.

The front score (FS) is a unitless variable used in this study to represent the strength of a frontal passage. FSs incorporate diurnal and elevation adjusted pressure rises and temperature falls over 30 minute intervals, calculated every five minutes so that the front score at 1230z compares station temperature and pressure at 1230z to the station temperature and pressure at 1200z. A 1mb pressure increase is considered the equivalent of 1K of temperature fall. Adding these differences together yields the front score (Eq. 3.15). An example of FSs at a station over several months is shown for JJA 1997 at the Blackwell Mesonet station (Fig. 3.2).

$$FS_{final} = T_{initial,diur.,elev.} + P_{final,diur.,elev.} - T_{final,diur.,elev.} - P_{initial,diur.,elev.} \quad (3.15)$$

FSs are used to determine whether or not a frontal passage occurs at a station or Mesonet triangle. A front is considered to have reached a Mesonet station when the FS at a station exceeds a minimum threshold. Also, the FS at the station must be the highest it reaches within 3 hours in either direction since it is common for the FS to stay above the threshold value for several consecutive timesteps. FSs of 3 and 5 are used as thresholds for fronts and strong fronts, respectively.

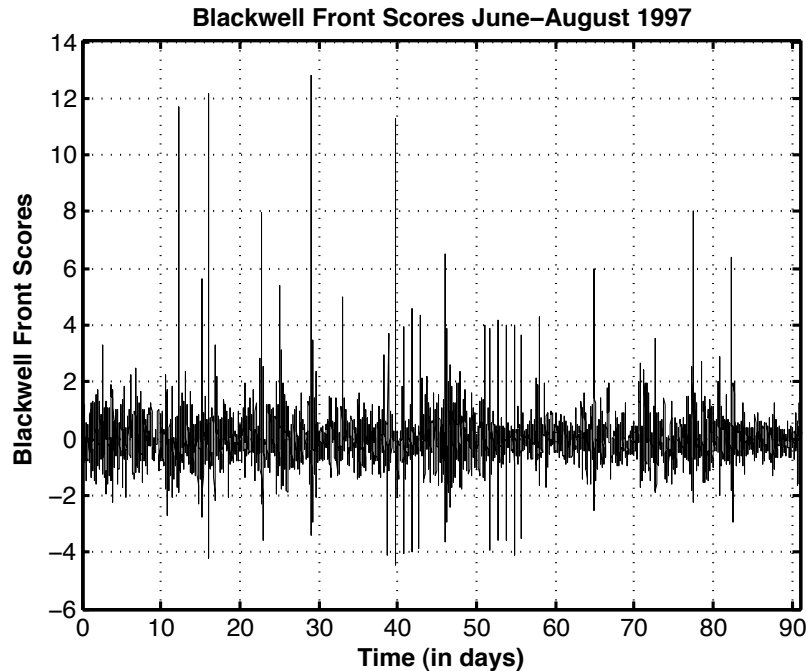


Figure 3.2 – Front scores for the JJA 1997 period at the Blackwell Mesonet station (36.75N, 97.25W). High, positive front scores indicate frontal passages.

A frontal passage at a Mesonet triangle is determined to have occurred if all three stations that comprise the corners of the triangle experience a frontal passage within a two-hour span. The two-hour limit is the reason that maximum triangle side length was limited to 80km since slower fronts are less likely to be observed in larger triangles leading to a low bias in front frequency. However, if the two-hour limit were extended more spurious fronts would have been captured. This limit was chosen in an effort to minimize the number of spurious fronts added and the number of legitimate fronts missed. The duration of the frontal passage at a triangle is from the time the first corner is reached by the front to the time the third corner is reached by the front. These fronts are assumed, due to lack of additional stations in the middle of the triangle, to have advanced at a constant speed as they progress through the Mesonet triangle. Additionally, these fronts can be tracked across the Mesonet as they progress in various case studies, detailed in Chapter 5.

3.4 Cold Pool Analysis

The frontal analysis is necessary in determining the location of potential convective cold pools since gust fronts mark the leading edge of cold pools (Wakimoto, 1982). Cold pools are primarily identified with temperature falls and pressure rises, much like the frontal passages themselves. Additionally, cold pools are regions of divergence which is the additional identifier used in this study to isolate fronts associated with cold pools from the rest of the frontal passages.

A cold pool is determined to have occurred at a Mesonet triangle if the triangle experiences a frontal passage and if strong divergence is present within half an hour before or an hour after the frontal passage reaches the timestep halfway through its progression through the triangle. The longer time duration after the frontal passage is due to cold pools being behind gust fronts. It is possible, given the resolution of the Mesonet grid, that a cold pool could seemingly be in place ahead of a front. Given the limitations in the resolution of the Mesonet grid, however, the possibility of a cold pool being present just before the front reaches the middle of the triangle is considered plausible. The strong divergence threshold is a divergence $> 10^{-4} s^{-1}$.

When a cold pool is determined to have occurred for the given frontal passage the duration of the cold pool is calculated. This is done by finding the divergence maximum and moving in both directions through time from the timestep of the divergence maximum until the divergence falls below half the maximum divergence value for that triangle.

Case studies are looked at using radar composite images from the National Center for Atmospheric Research (NCAR) image archive for the southern plains in Chapter 5. Statistics can be calculated for the fronts and cold pools identified by these methods and are detailed in Chapter 6.

CHAPTER 4

RESULTS: MASS FLUXES AND PRECIPITATION

4.1 Mass Fluxes

For the 15-yr dataset M_u , M_d , M_u^+ , and M_d^+ were calculated as averages over the entire Mesonet domain. Monthly averages were computed and a slight annual cycle can be observed where in the spring months the magnitude of the variables are, more often than not, larger in magnitude than the other seasons (Fig. 4.1).

The annual cycle for M_u , M_d , M_u^+ , and M_d^+ was calculated with the means and ranges found (Fig. 4.2). For all four variables the divergence or convergence magnitude is largest in the spring. The magnitude is lowest in September for the updraft variables and around November/December for downdrafts. For M_u and M_d the difference between the highest and lowest monthly averages is approximately 10%. For M_u^+ and M_d^+ the difference is approximately 20%. The seasonal cycle is strong enough that there is at least one month for each variable where all 15 years of values that month were below the average of another month, and a month where all 15 values were above the average of another month. For example, in Fig. 4.2a the lowest April value was higher than the mean value of all months from July through February, while all November values were lower than the mean values for March through June.

4.2 Precipitation

Precipitation values were also calculated for the 15-year dataset (Fig. 4.3). June 2007 was the wettest month at 8.56mm/day. No other month exceeded 7mm/day. The driest months were January 2003 and August 2000 with values of .061mm/day and .072mm/day respectively (Fig. 4.3a). June and May are the wettest months on average, while December through January are the driest on average (Fig. 4.3b).

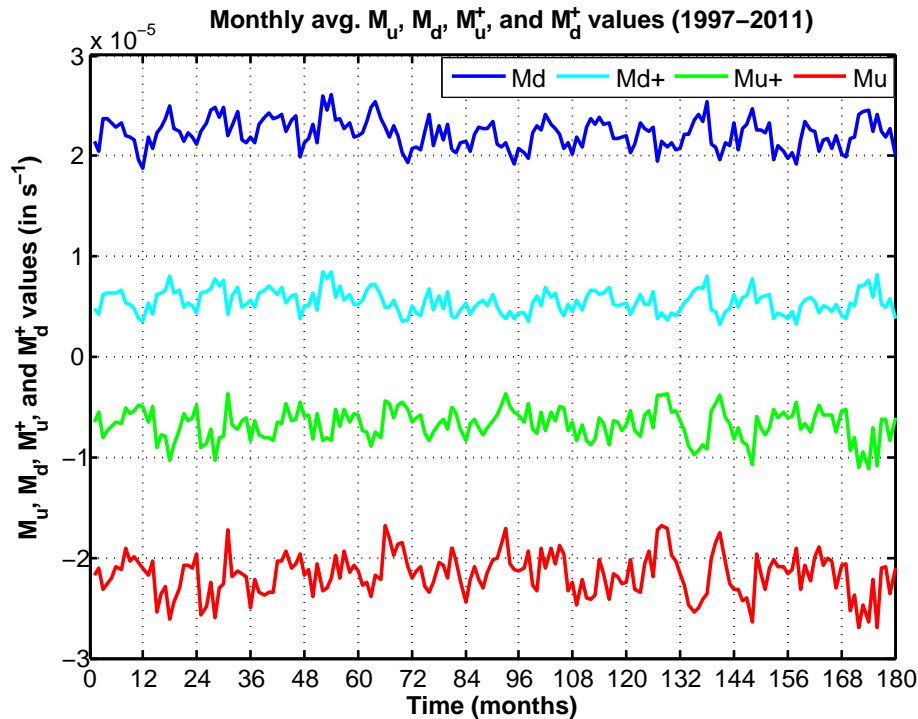


Figure 4.1 – Oklahoma Mesonet monthly values for M_u (green), M_d (cyan), M_u^+ (red), and M_d^+ (blue) over the 1997-2011 period. These values are averaged over the entire Mesonet area. Since stronger divergence/convergence is a subset of all convergence/divergence M_u^+ and M_d are higher in magnitude than M_u and M_d .

Despite the annual cycle, each month had a year with less than 1.5mm/day of rain and a year where the month had more than 3mm/day a result of the large variability from year to year in Fig. 4.3a.

Correlations were then calculated between the 3-hr averaged updraft/downdraft and Mesonet precipitation variables for the 15 year period (Table 4.1). Correlations between updrafts and downdrafts were higher in the summer (JJA, 0.53) than the other seasons (0.31, 0.28, 0.24). Likewise, strong updraft correlations were higher in the summer though by a smaller margin. Updrafts and downdrafts had higher correlations with Mesonet precipitation during the spring and summer and had the lowest correlations in the winter. The seasonal disparity is likely a result of the seasonal pattern of convective vs stratiform precipitation where convective precipitation is more common in summer while stratiform precipitation is more common in winter. M_u^+ and M_d^+ have a higher correlation with precipitation than do M_u and M_d .

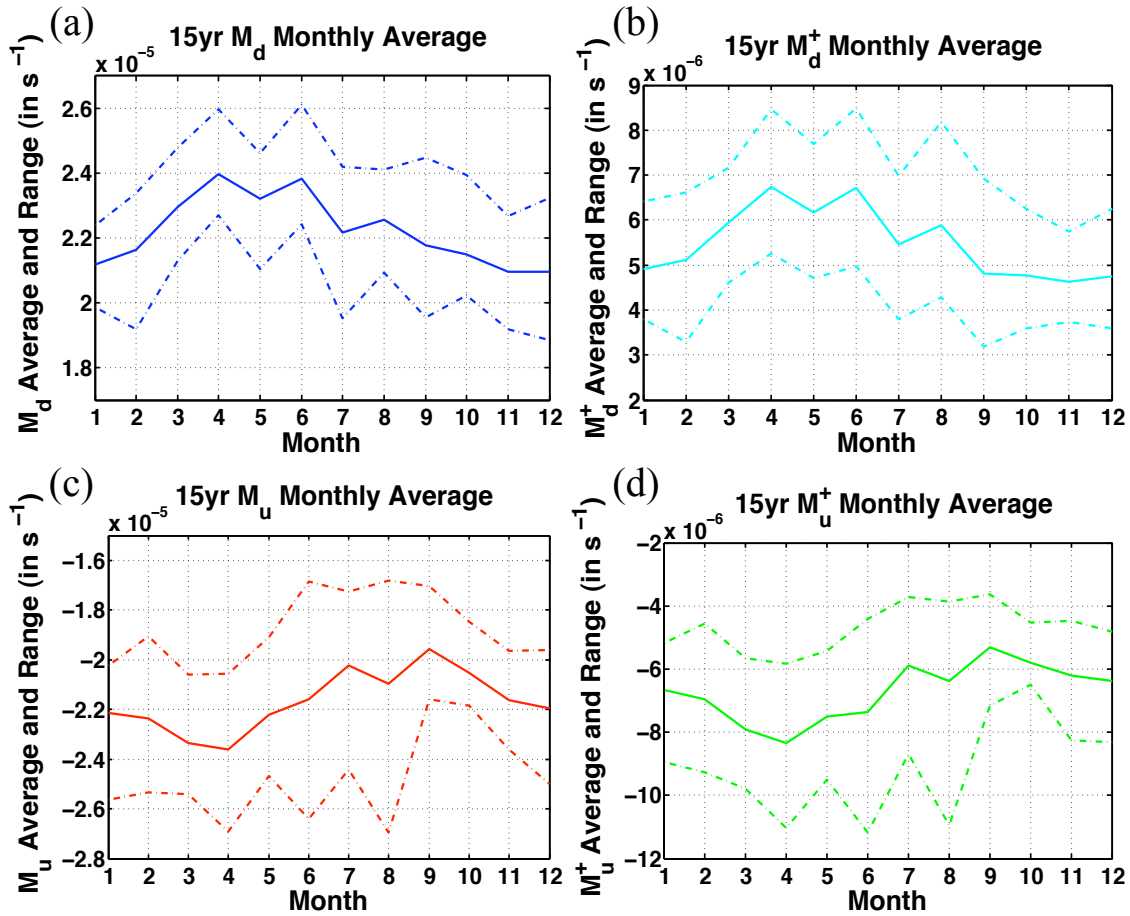


Figure 4.2 – Annual cycle of (a) M_d , (b) M_d^+ , (c) M_u , and (d) M_u^+ values for the Oklahoma Mesonet with the average and range plotted. Divergence and convergence are stronger on average in spring than the other seasons while convergence is weakest in September and divergence weakest in November/December.

Table 4.1 – Correlation table for each of the 4 seasons using the 15-yr of Mesonet observations for M_u , M_d , M_u^+ , M_d^+ , and precipitation (Prec).

Correlation	$M_u M_d$	$M_u^+ M_d^+$	$M_u \text{Prec}$	$M_d \text{Prec}$	$M_u^+ \text{Prec}$	$M_d^+ \text{Prec}$
Spring	0.31	0.69	0.43	0.42	0.49	0.55
Summer	0.53	0.78	0.48	0.48	0.55	0.59
Fall	0.28	0.67	0.40	0.31	0.46	0.44
Winter	0.24	0.65	0.26	0.17	0.31	0.27
Annual	0.35	0.70	0.40	0.37	0.46	0.49

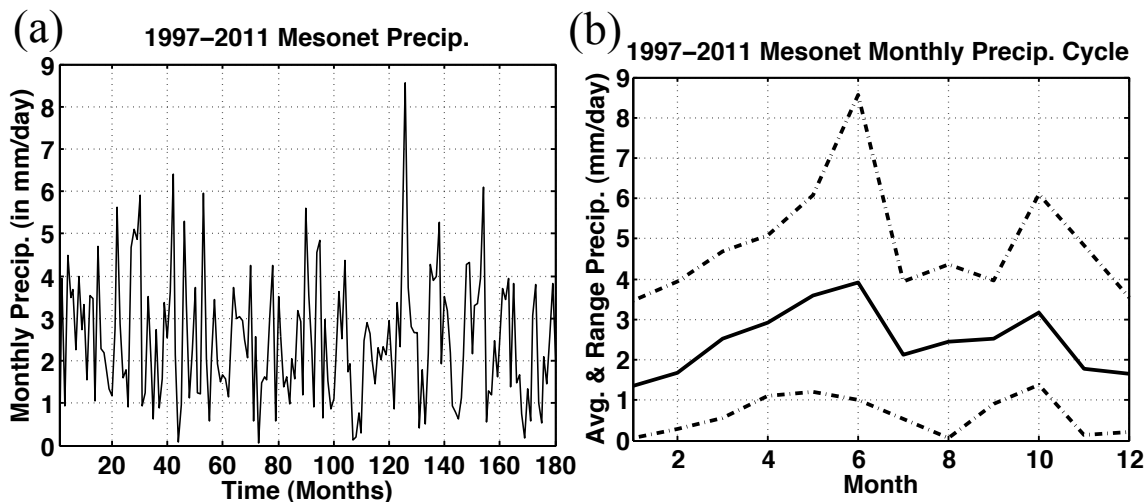


Figure 4.3 – Oklahoma Mesonet (a) monthly average precipitation values over the 1997-2011 period and (b) the monthly averages and range of the annual cycle of precipitation.

The influence of convection on updrafts and downdrafts was measured by comparing dry and wet days. Dry days are defined as days with 0mm of precipitation averaged over the Mesonet. Wet days are defined as days with at least 1mm of precipitation averaged over the Mesonet. This leaves days with 0.01-0.99mm of precipitation out which allows for more clarity between the two groups. Results show that wet days have stronger convergence than dry days, as expected (Fig. 4.4). Wet days in the spring and summer had the highest average updrafts and downdrafts. Additionally, summer dry days had the lowest average updrafts and downdrafts giving summer the largest disparity between wet and dry day averages. Winter had the lowest disparity between wet and dry day updraft and downdraft averages. Standard deviations were larger for wet days than dry days. This is largely a result of wet days including everything from showers to intense squall lines.

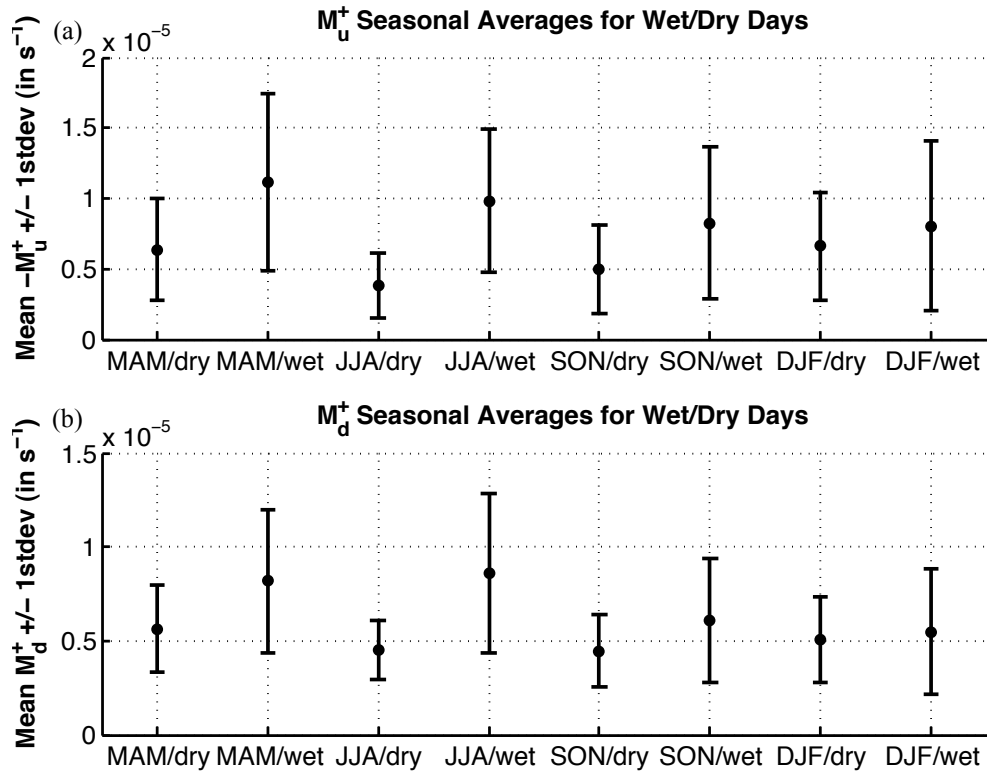


Figure 4.4 – Seasonal average and 1stdev. for (a) M_u^+ and (b) M_d^+ for wet (Mesonet area averaged precip. $> 1\text{mm}$) and dry (0 precip.) days. Wet spring and summer days have the strongest average updrafts and downdrafts while dry summer days have the weakest.

CHAPTER 5

RESULTS: CASE STUDIES

Over the 15 years of Mesonet data, tens of thousands of frontal passages at triangles were detected in the Oklahoma Mesonet with up to dozens of triangles reached with each front leaving hundreds of events that can be used for case studies. Four such cases will be shown in this section: 1) 13 June 1997, 2) 15-16 June 2002, 3) 20 May 2011, and 4) 24-25 May 2011. These cases are supplemented with radar images from the UCAR image archive.

5.1 13 June 1997 Case

Around 0 UTC on 13 June 1997 a squall line, which initiated in southeastern Colorado and northeastern New Mexico, was entering Kansas, the Oklahoma panhandle, and Texas. The disorganized line of thunderstorms entered Oklahoma at roughly 3 UTC and was tracked for the next 7 hours across the Mesonet (Fig. 5.1) with isolated thunderstorms popping up ahead of the main line. At 0330 UTC (Fig. 5.1a) the frontal analysis found only smaller segments of a front (yellow and magenta segments for fronts and strong fronts, respectively) in the northwest and center-west portions of Oklahoma. The radar images show a gap between two thunderstorms that coincides with the lack of strong convection (red dots on the figure). In the areas where a front was defined, convergence was present to the east ahead of the front and divergence to the west behind the front. Cold pools were able to be tracked as well (Fig. 5.2) though at 0330 UTC (Fig. 5.2a) there was only one triangle designated as in a cold pool, in the northwestern corner of the Mesonet domain.

From the 5 UTC frontal analysis (Fig. 5.1b), the stronger more well-defined front marks the leading edge of the system which had been organizing over the previous two hours. There was some bowing of the front present with trailing stratiform

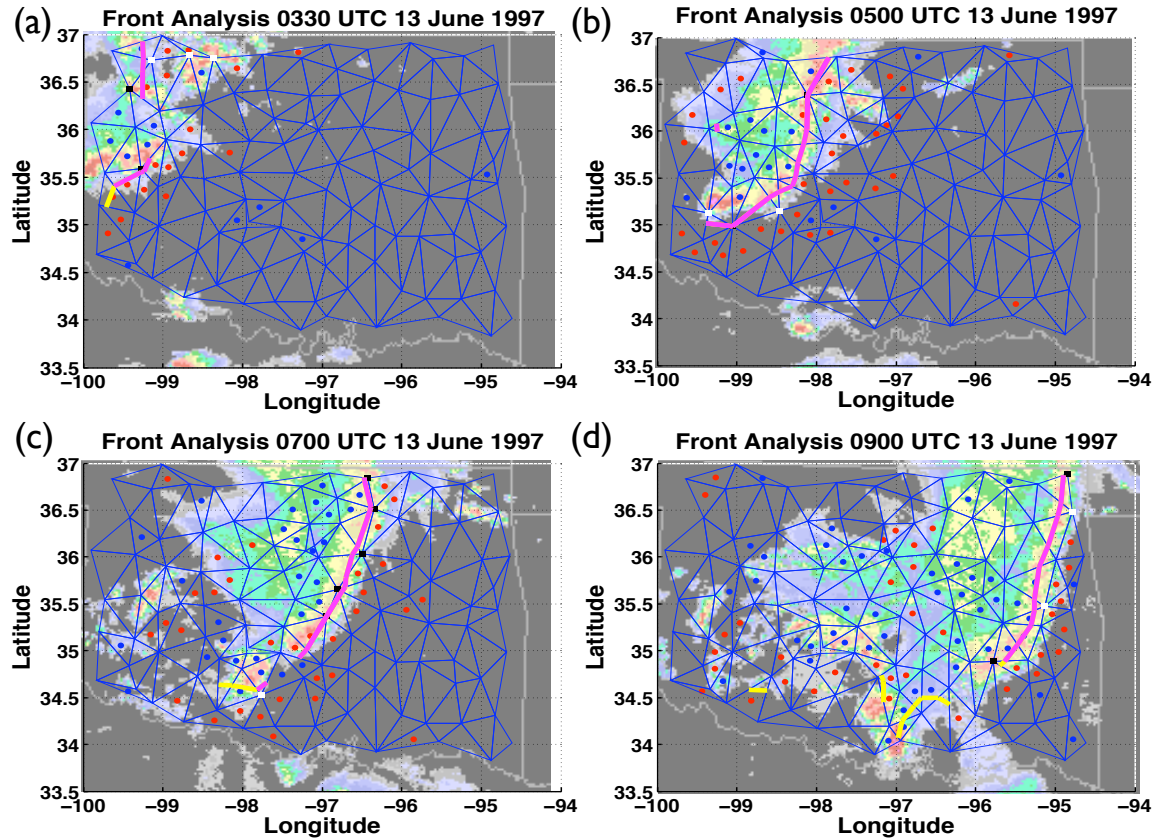


Figure 5.1 – Front analysis for 13 June 1997 (a) 0300 UTC, (b) 0500 UTC, (c) 0700 UTC, and (d) 0900 UTC. Red dots are convergence $> 10^{-4} s^{-1}$ while blue dots are divergence $\geq 10^{-4} s^{-1}$. Yellow lines are fronts where the three corners of the triangle have FSs of 3+ during frontal passage while magenta lines are fronts where the triangle corners have FSs are 5+. White squares are stations where at the current timestep the FS is $3 \leq FS < 5$; black squares designate stations currently with FSs at 5+. Radar images are from the UCAR image archive.

precipitation. The squall line had caught up to the isolated thunderstorms that developed ahead of the line. The area ahead of the front had strong convergence while strong divergence was present behind the front. Farther behind the front, near the back edge of the stratiform precipitation, there was a second region of convergence where a one-triangle front is marked. The analysis was designed to capture the strongest fronts at each triangle and in this case this latter front was stronger than when the initial line passed through heading eastward. This was likely a result of the squall line being somewhat disorganized in that area at the time it passed that particular triangle. A large cold pool stretched from the main squall line front to the

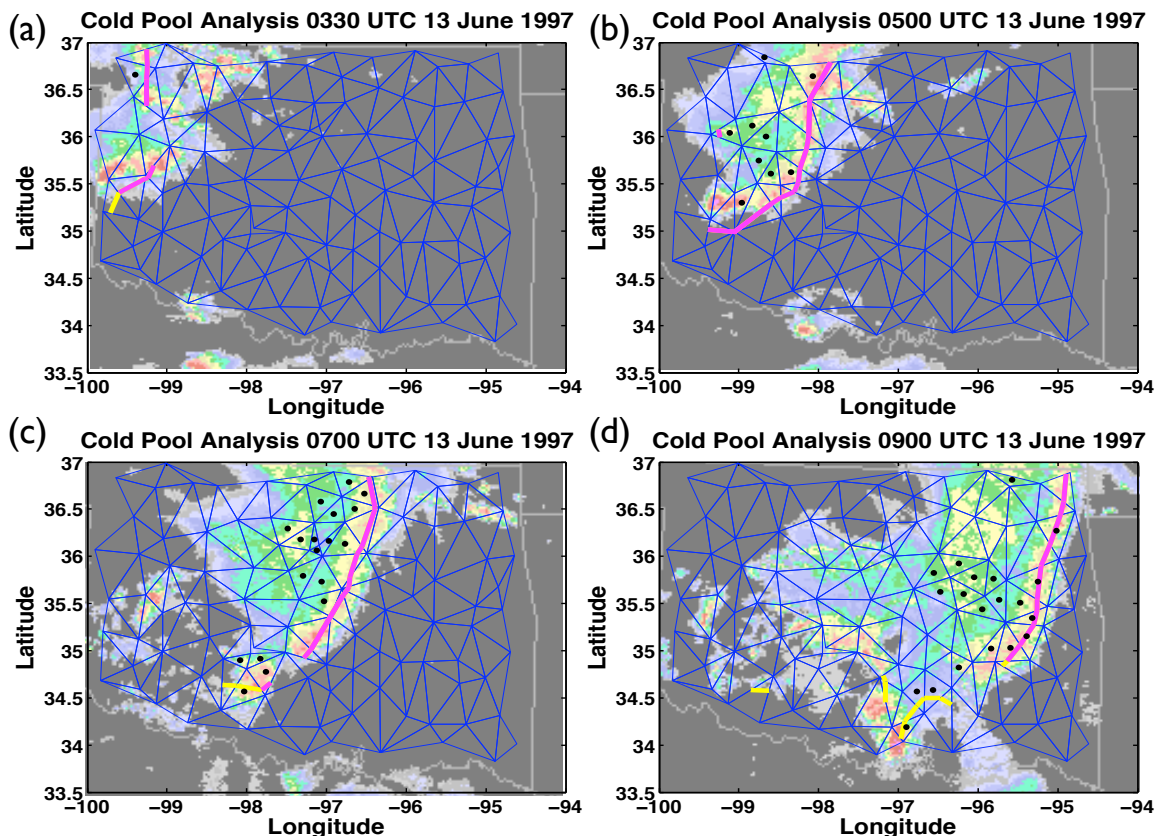


Figure 5.2 – Cold pool analysis for 13 June 1997 (a) 0330 UTC, (b) 0500 UTC, (c) 0700 UTC, and (d) 0900 UTC. Black dots mark triangles that are in cold pools at this time. Fronts from Figure 5.1 are shown for context. Radar images are from the UCAR image archive.

back edge of the stratiform precipitation (Fig 5.2b) in west-central Oklahoma.

From 5 to 7 UTC, the supercell at the south end of the squall line separated from the rest of the line. This separation appears in the form of a gap in the front that was a result of lower FSs (Fig. 5.1c). The southern cell has weaker FSs as one of the triangles marked by the front only meets the lower front score threshold of 3 rather than the higher threshold of 5. The region of strong divergence was primarily concentrated in north central Oklahoma, with a smaller area of strong divergence behind the southern supercell. Cold pools are located in both of these areas (Fig. 5.2c). In Western Oklahoma a few small convective cells had formed behind the secondary convergence line.

By 9 UTC the southern supercell had progressed southeastward much farther

away from the rest of the line (Fig. 5.1d). The stronger portion of the front led the main squall line eastward. The area of strong divergence behind the front was more concentrated on the southern half of the squall line. There was a weaker front (FSs 3+ rather than 5+) to the east of the southern supercell. Behind the supercell to the northwest, trailing convection developed over the previous two hours and eventually joins with the southern supercell (not pictured). There was clear separation between the convergence and divergence in the trailing convection. Overall, the frontal analysis using FSs performed well at representing the location of the front that would be expected based on the radar images. Despite the separation in the front, the cold pool along the front almost extends from the southern border with Texas to the northern border with Kansas (Fig. 5.2d). Notably the cold pool extends far back behind the front in east-central Oklahoma, suggesting a very long-lived cold pool. At this time, the main cold pool has been in place for hours and has advanced eastward over time behind the squall line.

Observing the change in cold pool area over time allows for greater visualization of the size and time scales of the areas experiencing a cold pool (Fig. 5.3). From roughly 3 to 11 UTC at least one Mesonet triangle resided in a cold pool. The peak size of cold pool area was around 930 UTC at a size of roughly $1.6E^{10}m^2$. Around a third of the cold pool areas retained a cold pool for at least 30 minutes, and some triangles, particularly later in the period, retained cold pool status for over an hour.

5.2 15-16 June 2002 Case

Around 18 UTC 15 June, a line of thunderstorms oriented from northwest to southeast was located in north central Kansas and south central Nebraska moving southeast. Over the next few hours the system spread out along the front allowing for a much more southwest to northeast oriented storm line to develop as the system moved south to the Oklahoma border. The frontal passage (Fig. 5.4) and cold pool (Fig. 5.5) analysis for this event is shown.

At 0 UTC on the 16th the squall line had just entered the northwest corner of Oklahoma. Very strong convection was present ahead of the line, including triangles over 50 km ahead of the squall line (Fig. 5.4a). Divergence behind the front was

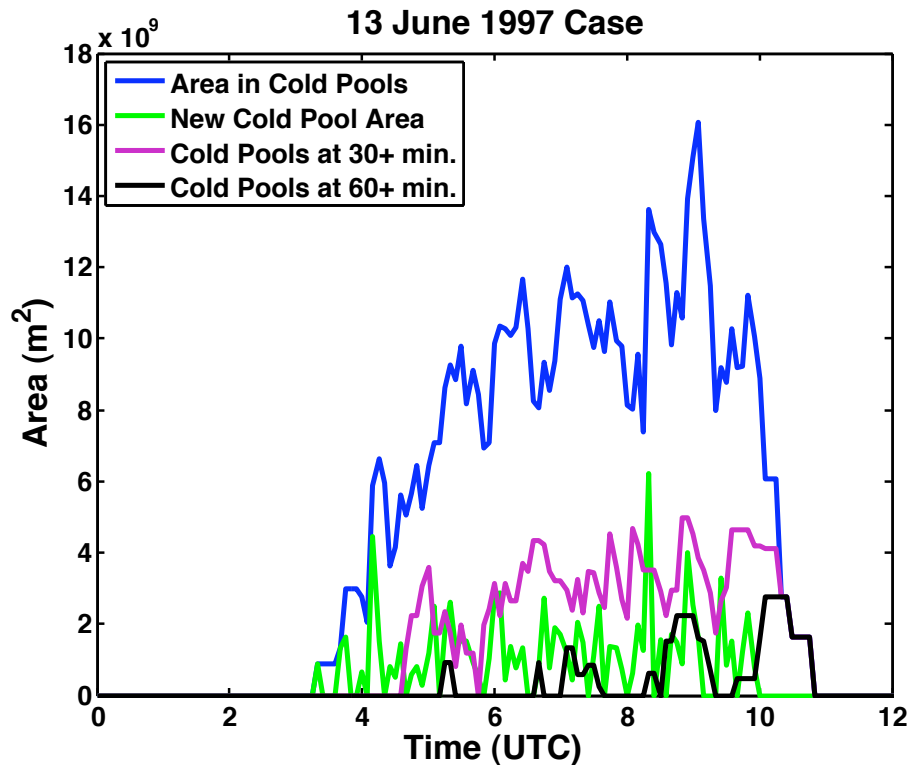


Figure 5.3 – Cold pool areas for the 13 June 1997 0-12 UTC case study. Cold pool areas are shown for total area in cold pools (blue), area that becomes part of a cold pool the given timestep (green), area that has been in a cold pool at least 30 minutes (purple), and area that has been in a cold pool at least 60 minutes (black).

present as well as this line had developed into a mature line several hours earlier. The FSs exceeded the strong front threshold. A few isolated triangles along and just behind the line were located in cold pools at this time (Fig. 5.5a). Presumably the cold pool extends into Kansas at this time.

Ninety minutes later the squall line had progressed into the state reaching from almost the southwest corner to the northeast corner of Oklahoma (Fig. 5.4b). The stronger radar echoes were in the western half of the squall line, matching up with the stronger FSs. Additionally, the convergence-divergence pattern ahead of and behind the front was more well-defined in the western half of the state though present throughout the squall line. A broad region of heavy stratiform precipitation was located in north central Oklahoma. In that stratiform precipitation region a cold

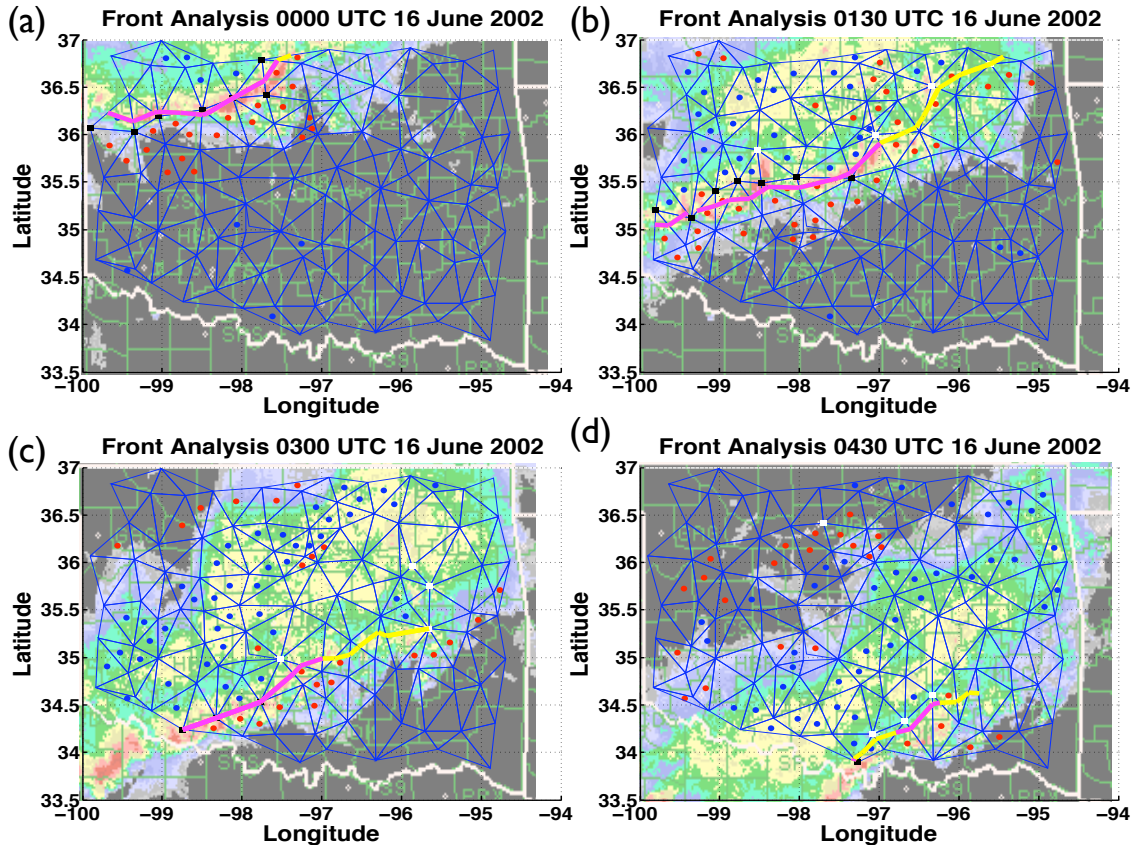


Figure 5.4 – Front analysis for 16 June 2002 (a) 0000 UTC, (b) 0130 UTC, (c) 0300 UTC, and (d) 0430 UTC. Red dots are convergence $> 10^{-4} s^{-1}$ while blue dots are divergence $\geq 10^{-4} s^{-1}$. Yellow lines are fronts where the three corners of the triangle have FSs of 3+ during frontal passage while magenta lines are fronts where the triangle corners have FSs are 5+. White squares are stations where at the current timestep the FS is $3 \leq FS < 5$; black squares designate stations currently with FSs at 5+. Radar images are from the UCAR image archive.

pool was detected far behind the squall line (Fig. 5.5b). Additionally, along the front there was a narrow band of scattered triangles that are in cold pool status, just behind strong convective cells.

By 3 UTC the eastern half of the squall line had lost much of its strong convection resulting in a front that does not extend all the way to the Arkansas border (Fig. 5.4c), or at least not a front strong enough to meet the minimum threshold in this study. The southwestern corner of Oklahoma still features strong convection, with the line extended into north central Texas. The eastern half of the state has lost most of

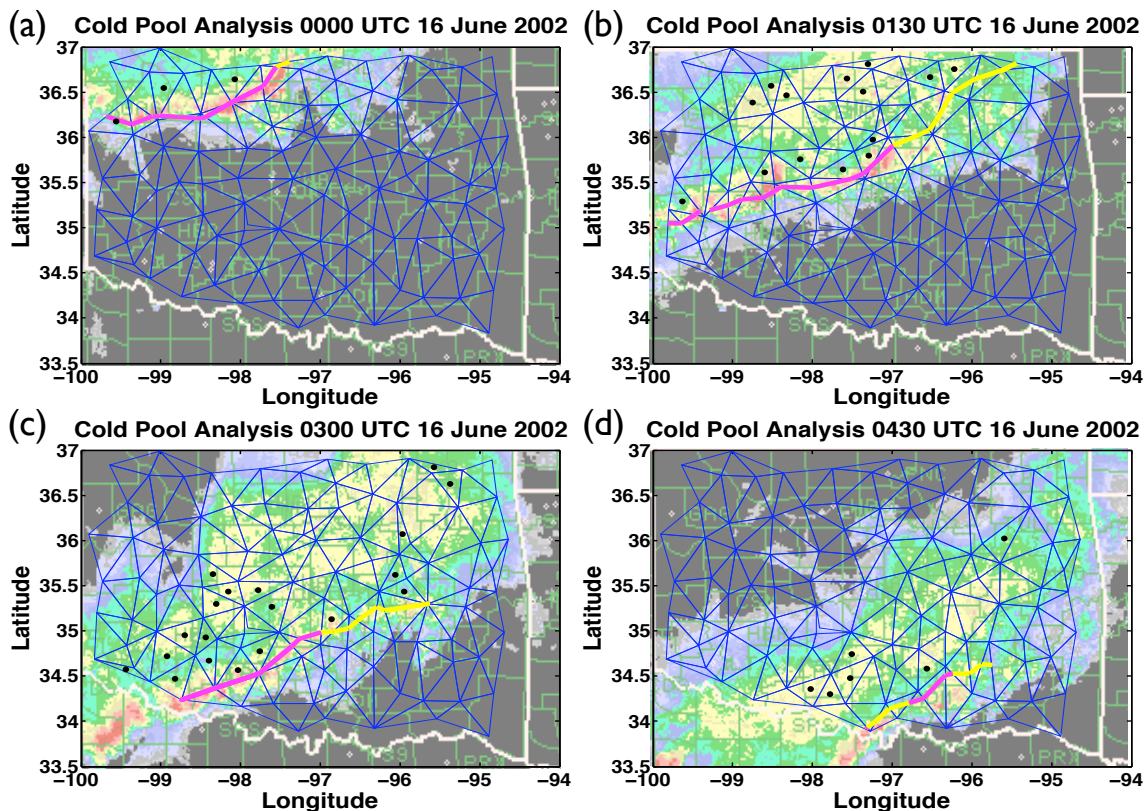


Figure 5.5 – Cold pool analysis for 16 June 2002 (a) 0000 UTC, (b) 0130 UTC, (c) 0300 UTC, and (d) 0430 UTC. Black dots mark triangles that are in cold pools at this time. Fronts from Figure 5.4 are shown for context. Radar images are from the UCAR image archive.

its divergence behind the line as the convective structure has fallen apart. However, there was still a narrow region of convergence ahead of the squall line. South central Oklahoma had a very large area of divergence behind the front. This extends up into north central Oklahoma with the trailing portion of the stratiform precipitation region. A small line of convergence was present in the stratiform precipitation region in north central Oklahoma with an additional larger line of convergence behind the stratiform precipitation. There are many triangles experiencing a cold pool in the south central Oklahoma behind the squall line (Fig. 5.5c). Extending back several triangles deep, this cold pool covers roughly one eighth of the state. The eastern half of the state has much less cold pool coverage though the cold pool does include a couple triangles in the northeast corner where the front had passed over an hour

prior.

As the system moves farther southeast the strength of the convection in Oklahoma weakened further as the strongest cells to the west moved into Texas. The stratiform region of precipitation was well-defined and contained a large area of divergence behind the remnants of the squall line in Oklahoma (Fig. 5.4d). The line of convergence that was just behind the stratiform precipitation region has fallen farther behind the precipitation though it maintains an almost continuous line through a large portion of the northwest to north central region. The cold pool was concentrated in the south central stratiform precipitation with a few solitary triangles elsewhere in cold pools (Fig. 5.5d).

The cold pool time series shows a slightly larger maximum cold pool area than the first case study with a maximum size of roughly $1.9E^{10}m^2$ (Fig. 5.6). The duration of the cold pools tended to be longer than the first case study. Later in the time period over half the cold pool area comprised of locations which had been in a cold pool for half an hour or more. Cold pool area that was present for at least an hour peaked at roughly $0.6E^{10}m^2$.

5.3 20 May 2011 Case

One of the more notable cases during the Mid-Latitude Continental Convective Clouds Experiment (MC3E) occurred on 20 May 2011 (Fig. 5.7). Scattered convective cells formed in central Oklahoma and by 4 UTC the cells stretched from the Oklahoma-Texas border southwest to the Texas panhandle. These cells organized into a squall line and started to build north through southwestern Oklahoma with the fronts and cold pools tracked with the algorithm (Fig. 5.8).

At 9 UTC (Fig. 5.7a) the frontal analysis shows a strong front stretching from southwestern Oklahoma northward to central Oklahoma. There was a well-defined squall line as well as convergence ahead of the front and areas of strong divergence behind the front. The structure of the line appears less organized at the northern end of the front as strong convection juts out ahead of the rest of the front. This was due to an isolated thunderstorm from earlier that was merging into the squall line. Due to the merging of that thunderstorm, the frontal boundary was not as well

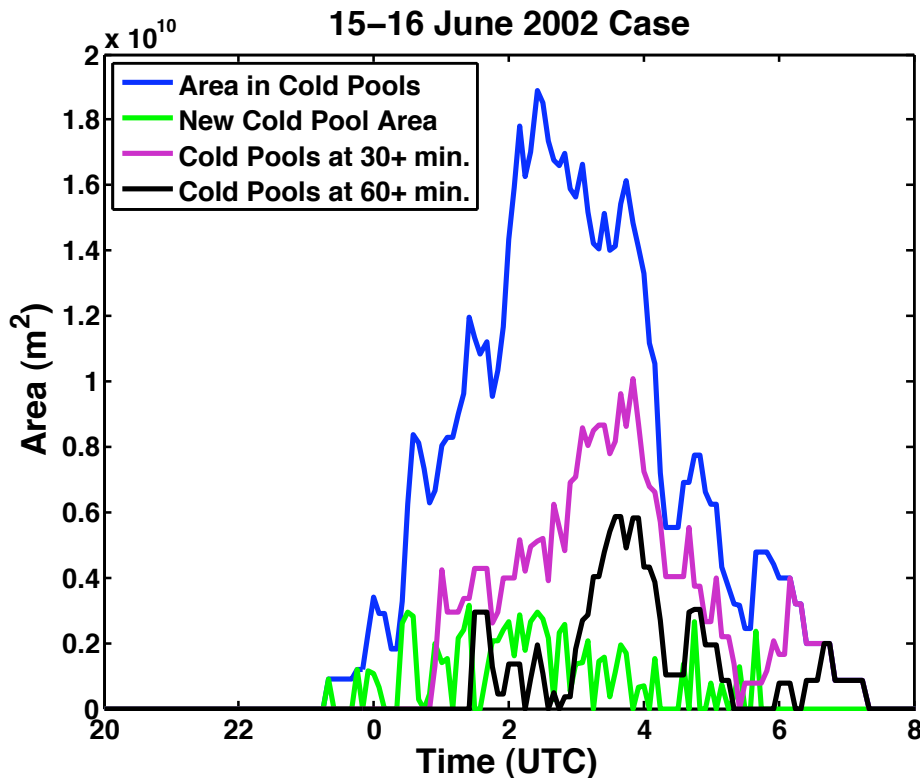


Figure 5.6 – Same as Figure 5.3, except for the 15-16 June 2002 20-8 UTC case study.

defined in that area and there was only some semblance of a convergence-divergence couplet. Since the line had just developed northward into the area the previous two hours, only two triangles have cold pools present at 9 UTC (Fig. 5.8a).

Over the next couple of hours the squall line builds throughout northern Oklahoma. By 11 UTC the line had developed a bow shape (Fig. 5.7b). Notably, the easternmost part of the bow has lower FSs and contained a break in the high convergence area as well as having slightly lower radar returns. However, a strong divergence area behind the line did remain intact in that region. The northern part of the squall line has convergence ahead of the front but the FSs at some stations were not high enough to trigger a front to be drawn in that area. Since the northern edge of the front was the most recent to form, it was not strong enough to meet minimum front score thresholds. A distinct line of triangles containing cold pools stretches through over two thirds the width of the state just behind the front (Fig.

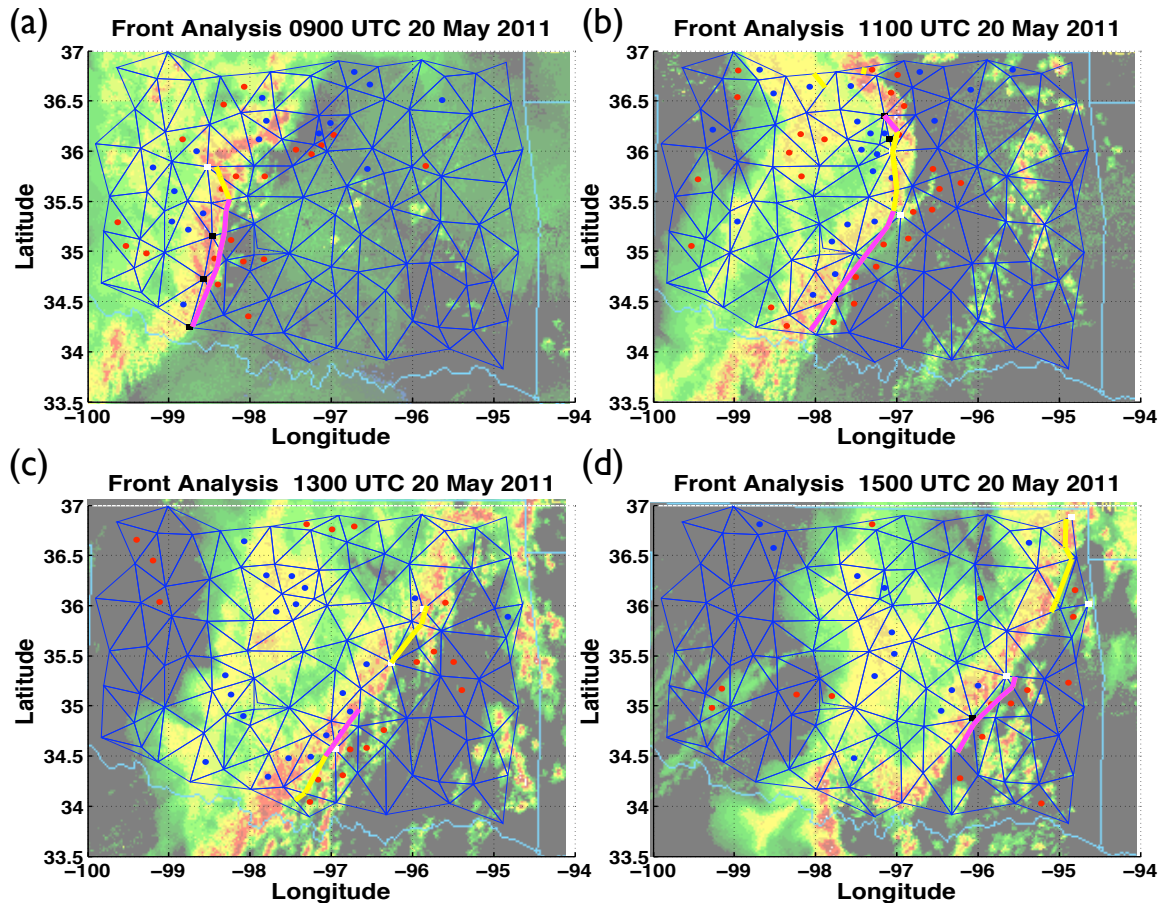


Figure 5.7 – Front analysis for 20 May 2011 (a) 0900 UTC, (b) 1100 UTC, (c) 1300 UTC, and (d) 1500 UTC. Red dots are convergence $> 10^{-4} s^{-1}$ while blue dots are divergence $\geq 10^{-4} s^{-1}$. Yellow lines are fronts where the three corners of the triangle have FSs of 3+ during frontal passage while magenta lines are fronts where the triangle corners have FSs are 5+. White squares are stations where at the current timestep the FS is $3 \leq FS < 5$; black squares designate stations currently with FSs at 5+. Radar images are from the UCAR image archive, NEXLAB - College of DuPage.

5.8b). Unlike the 1997 case, the cold pool does not extend as far behind the front.

From 11 to 13 UTC the northern part of the bow began to break apart. Convection ahead of the front led to a more scattered area of thunderstorms in northeastern Oklahoma (Fig. 5.7c) as well as thunderstorms popping up several counties east of the squall line. The structure of the line was oriented southwest to northeast by 13 UTC. The frontal analysis retained the southern half of the state's front as meeting the strong front threshold while a few triangles on the northern end have the lower

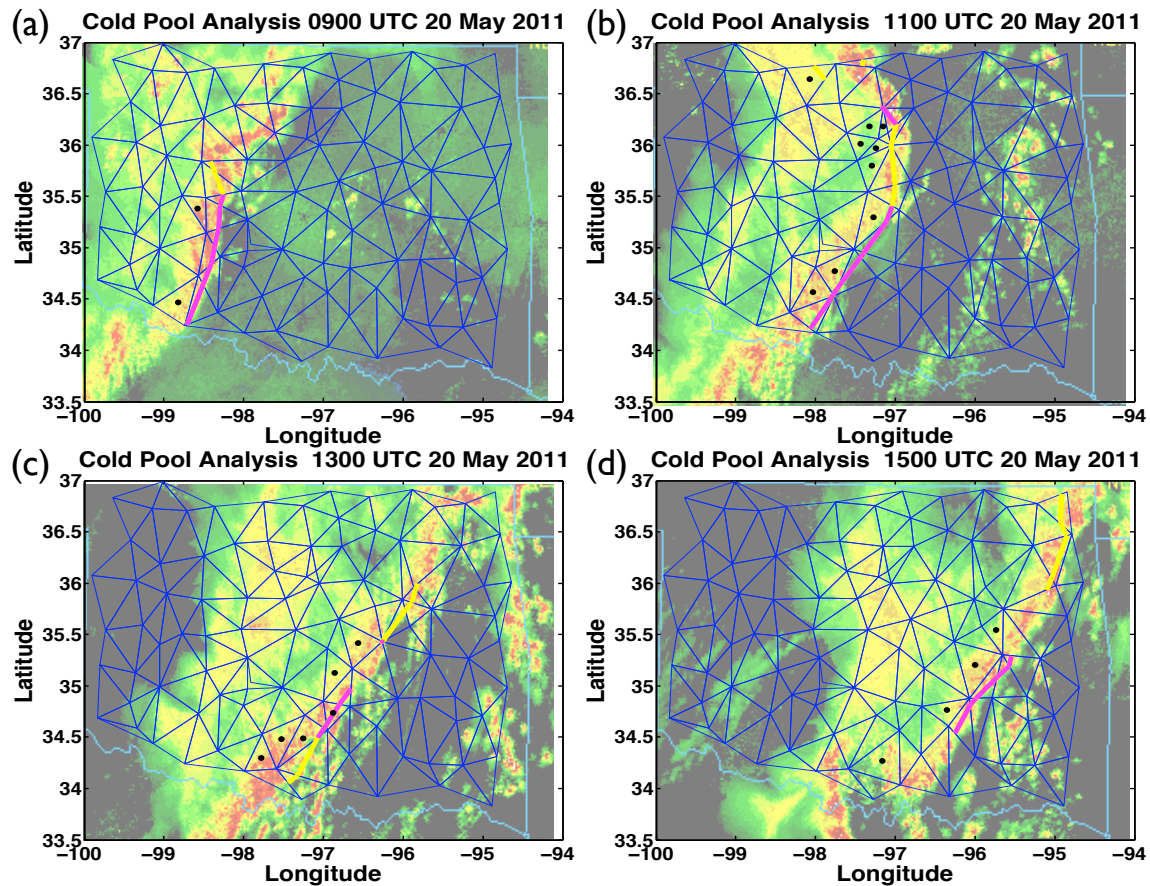


Figure 5.8 – Cold pool analysis for 20 May 2011 (a) 0900 UTC, (b) 1100 UTC, (c) 1300 UTC, and (d) 1500 UTC. Black dots mark triangles that are in cold pools at this time. Fronts from Figure 5.7 are shown for context. Radar images are from the UCAR image archive.

FS threshold met. Similarly the cold pool area has decreased as only the southern Oklahoma portion of the front managed to exceed the divergence threshold (Fig. 5.8c).

The front continues through the state, exiting through northeastern Oklahoma around 15 UTC (Fig. 5.7d) while the southern end exits the state hours later before a second line of storms moves into southeastern Oklahoma (not shown). There was little divergence behind the northeastern Oklahoma portion of the front. The cold pool covered only a few triangles in southeastern Oklahoma (Fig. 5.8d).

The cold pool time series showed a longer lasting period from initial to final cold pool and a lower maximum cold pool area that only reached roughly $0.9E^{10}m^2$ (Fig.

5.9). There are frequent jumps in the amount of area covered by cold pools. Many of the cold pools lasted half an hour; however, very few triangles maintained a cold pool for at least an hour. Considering the narrow width of the divergence region behind the storm line and the speed of the front, this result was expected.

5.4 24-25 May 2011 Case

The final case study is another system that occurred during the MC3E experiment a few days after the previous case. On 24 May the 18 UTC sounding (not shown, UCAR archive) from Norman, Oklahoma (KOUN) had strong southerly winds at low-levels veering with height. A strong stable layer at roughly 825 mb was in place; however, low-level moisture and an unstable mid-level resulted in CAPE values over 2500 Jkg^{-1} . The Storm Prediction Center (SPC) had issued a high risk convective outlook for central and northeastern Oklahoma.

By 20 UTC the first thunderstorm cells had formed, rapidly developing into severe thunderstorms with a threat of tornadoes. The frontal passage (Fig. 5.10) and cold pool (Fig. 5.11) analysis had some difficulty capturing the front and any associated cold pool with these thunderstorms due to the low resolution of the Mesonet station grid (Fig. 5.10a). There was a large region of convergence both ahead of and behind the supercells at this time. The front, although strong, did not extend throughout all of the supercells, and only one triangle observed a cold pool (Fig. 5.11a).

Over the next couple hours, more cells had flared up and a clear north-south line had formed (Fig. 5.10b) though there were gaps between the cells that made up the line. There was only a slight signature of the usual convergence-divergence pattern ahead of and behind the front, likely, though not necessarily, a result of the strong rotation in tornadoes, or systems capable of potentially producing tornadoes. At this point multiple tornadoes had formed including one which struck the El Reno Mesonet station at 2120 UTC recording a maximum wind gust of 151 mph. Only a few stations in north central and northwestern Oklahoma observed cold pools at the time (Fig. 5.11b). Strong rotation tends to lead to surface inflow from all directions, reducing the likelihood of divergence and cold pools behind a front.

By 0 UTC, however, the squall line was straighter and had fewer, smaller gaps

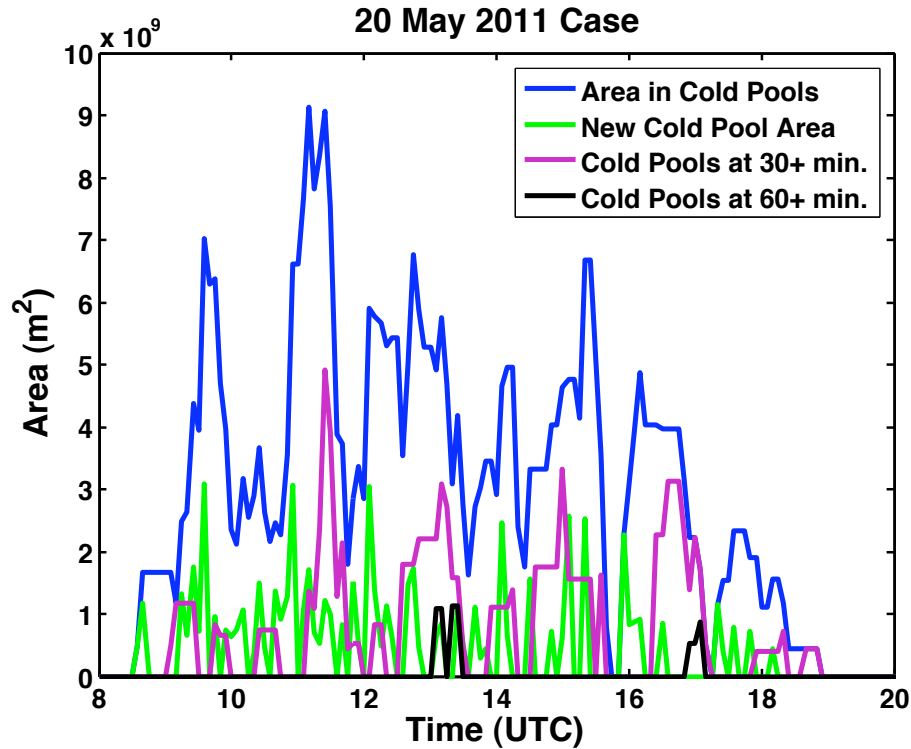


Figure 5.9 – Same as Figure 5.3, except for the 20 May 2011 8-20 UTC case study.

between individual storm cells (Fig. 5.10c). A convergence-divergence distribution ahead of and behind the front was more well-defined in the north central Oklahoma line and the smaller, weaker (in terms of front strength) line in south central Oklahoma. A large region of convergence is present in western Oklahoma where a secondary front was present that lacked precipitation. Cold pool coverage had grown behind the main line in central Oklahoma (Fig. 5.11d). Additionally, one triangle was marked as in a cold pool in the northwest corner of Oklahoma.

As the main front progressed further eastward the strength of the front began to weaken slightly with regards to FSs (Fig. 5.10d). However, convection was still intense with radar echoes reaching up to 60 dBZ still present. The fronts in western Oklahoma had a disorganized structure and covered more area at the time. The cold pools at 2 UTC remained just behind the main front with one triangle in western Oklahoma in a cold pool as well (Fig. 5.11d). Radar coverage in northwestern Oklahoma was sparse by comparison, though the secondary line does not appear to

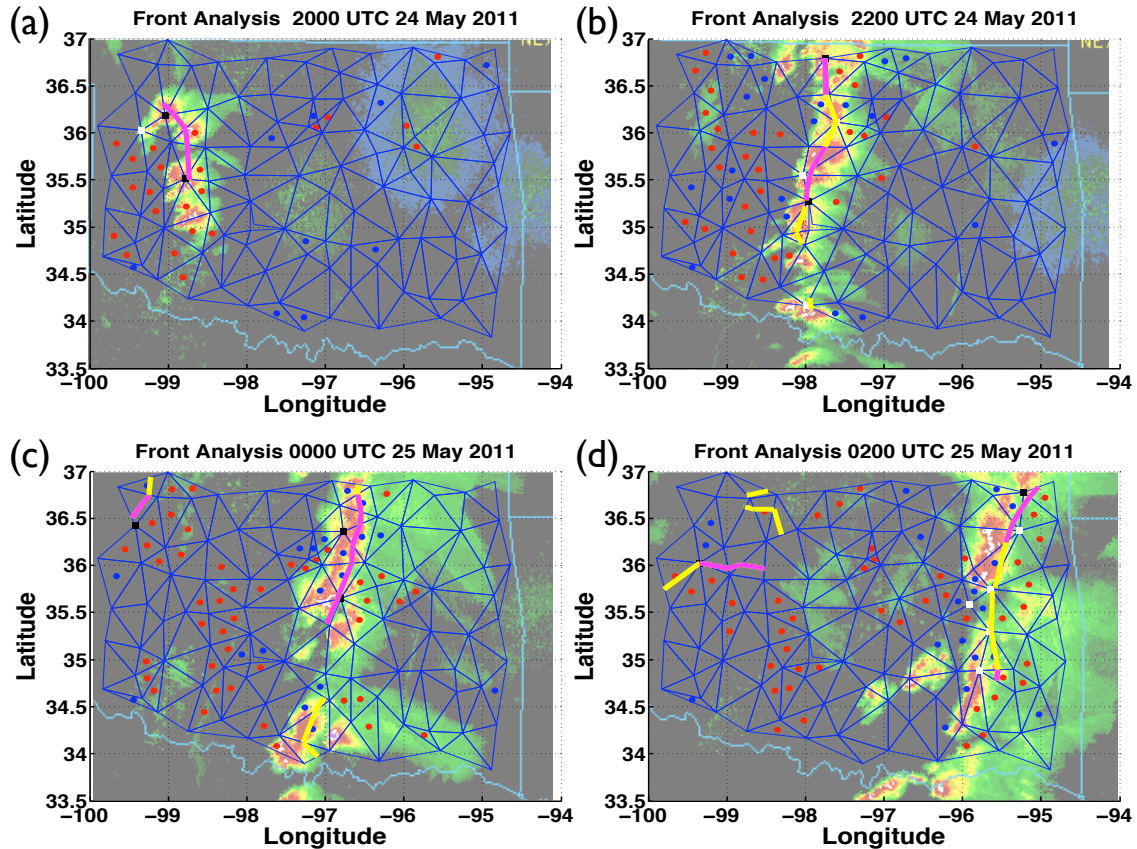


Figure 5.10 – Front analysis for 24 May 2011 (a) 2000 UTC, (b) 2200 UTC, 25 May 2011 (c) 0000 UTC, and (d) 0200 UTC. Red dots are convergence $> 10^{-4} s^{-1}$ while blue dots are divergence $\geq 10^{-4} s^{-1}$. Yellow lines are fronts where the three corners of the triangle have FSs of 3+ during frontal passage while magenta lines are fronts where the triangle corners have FSs are 5+. White squares are stations where at the current timestep the FS is $3 \leq FS < 5$; black squares designate stations currently with FSs at 5+. Radar images are from the UCAR image archive, NEXLAB - College of DuPage.

develop precipitation as it moves throughout the state the next few hours. At 3 UTC (not shown) there was a faint green line visible on the radar signifying this secondary front.

The cold pool time series for this final case study showed a maximum cold pool area of just over $1.1E^{10} m^2$ (Fig. 5.12). The entire period with cold pools present lasted approximately 10 hours. The cold pools were rather short in duration with few lasting half an hour and only one triangle retaining a cold pool over an hour. Cold pools later in the event had longer durations than cold pools in the first half of the

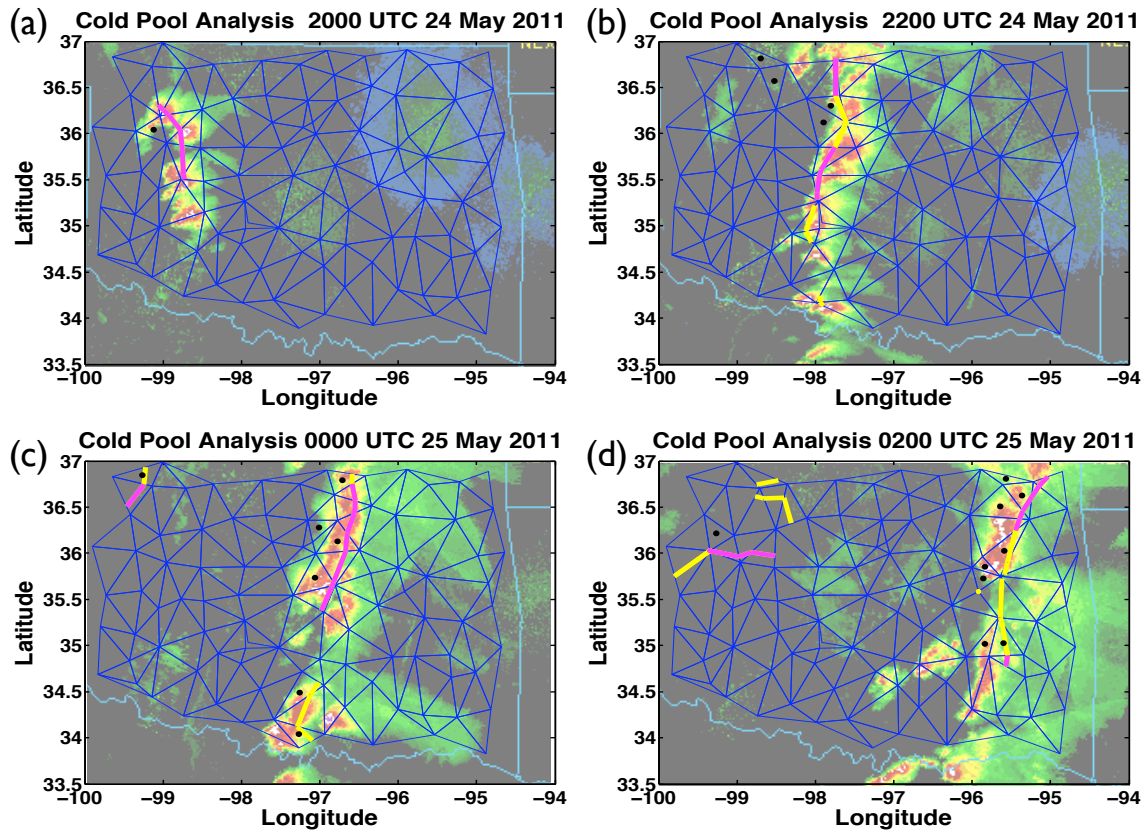


Figure 5.11 – Cold pool analysis for 24 May 2011 (a) 2000 UTC, (b) 2200 UTC, 25 May 2011 (c) 0000 UTC, and (d) 0200 UTC. Black dots mark triangles that are in cold pools at this time. Fronts from Figure 5.10 are shown for context. Radar images are from the UCAR image archive.

event, a result of the increased organization of the convergence-divergence gradient across the front over time.

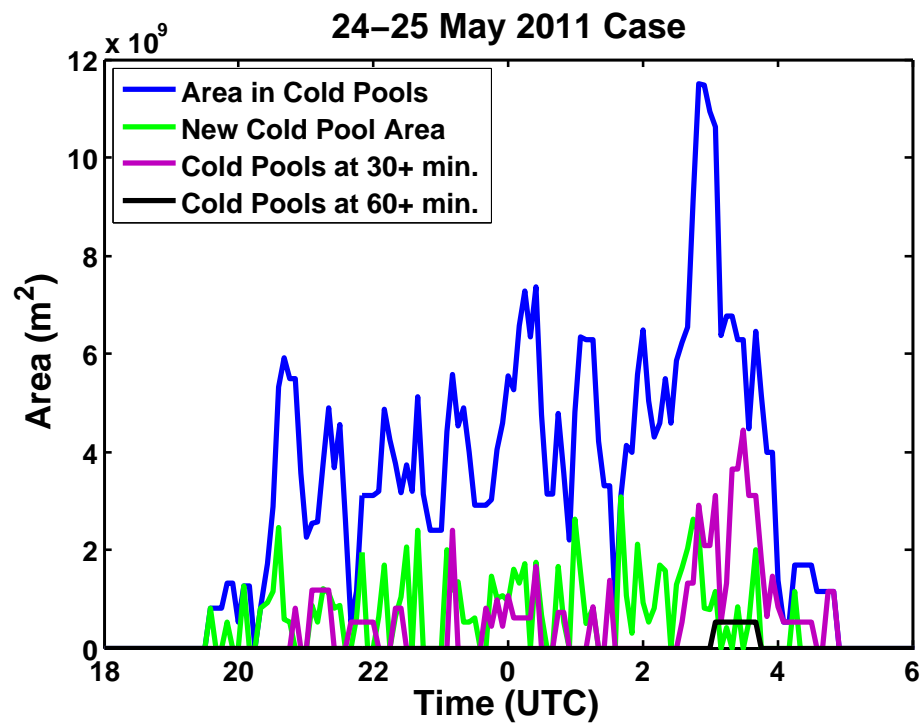


Figure 5.12 – Same as Figure 5.3, except for the 24-25 May 2011 18-6 UTC case study.

CHAPTER 6

RESULTS: 15-YEAR CLIMATOLOGY OF FRONTS AND COLD POOLS

The 1997-2011 period of Oklahoma Mesonet data allowed for 15 years of frontal passages and cold pools to be analyzed with statistics gathered on these frontal passages and frontal passages connected with cold pools. This analysis processed almost one billion observations from the Mesonet. Frontal passage and cold pool statistics are covered for: 1. Variable changes (T , P , q_v , and hcp^{-1}), 2. Convergence/divergence 3. Seasonal distribution, 4. Diurnal distribution, and 5. Geographic distribution.

6.1 Variable Changes (T , P , q_v , and hcp^{-1})

For each frontal passage at a Mesonet triangle the three corners of the triangle were included in the statistics of changes in key variables as a result of the frontal passage. Those variables are temperature (T), pressure (P), water vapor mixing ratio (q_v), and moist static energy in temperature units (hcp^{-1}). The changes in these four variables during all frontal passages (FS3+) and strong frontal passages (FS5+) (Table 6.1) and frontal passages that result in cold pools and strong cold pools are shown (Table 6.2).

The temperature difference is calculated by subtracting the highest temperature within 30 minutes before a frontal passage at a station from the lowest temperature within 2 hours after the frontal passage. Pressure differences are calculated by subtracting the lowest pressure within 30 minutes before the frontal passage from the highest pressure within 2 hours after the frontal passage. The times before and after the front are not necessarily the same for temperature and pressure changes. Δq_v and Δhcp^{-1} , however, are calculated at the same timestep as ΔT . This was chosen because T and q_v are directly involved in calculations of hcp^{-1} .

Table 6.1 – Average ΔT , ΔP , Δq_v , and Δh_{cp}^{-1} for all frontal passage (FS3+ / FS5+).

Season	ΔT (K)	ΔP (mb)	Δq_v (gkg ⁻¹)	Δh_{cp}^{-1} (K)
Spring (MAM)	-5.8/-7.7	2.8/3.6	-1.5/-2.9	-9.2/-14.8
Summer (JJA)	-6.1/-7.7	2.0/2.5	-0.6/-1.0	-7.1/-10.2
Fall (SON)	-6.2/-8.4	2.4/3.1	-1.5/-2.8	-9.6/-15.3
Winter (DJF)	-6.6/-10.2	2.9/4.4	-1.2/-2.7	-9.5/-17.1
Annual	-6.1/-8.1	2.5/3.2	-1.1/-2.1	-8.7/-13.4

Table 6.2 – Average ΔT , ΔP , Δq_v , and Δh_{cp}^{-1} during frontal passages that yield cold pools (FS3+ / FS5+).

Season	ΔT (K)	ΔP (mb)	Δq_v (gkg ⁻¹)	Δh_{cp}^{-1} (K)
Spring (MAM)	-5.8/-7.5	2.9/3.5	-1.7/-2.8	-10.1/-14.6
Summer (JJA)	-6.2/-7.7	2.0/2.5	-0.8/-1.0	-8.1/-10.3
Fall (SON)	-6.3/-8.3	2.6/3.1	-1.6/-2.5	-10.3/-14.6
Winter (DJF)	-7.1/-10.3	3.5/4.5	-1.5/-2.8	-10.9/-17.1
Annual	-6.2/-8.0	2.6/3.1	-1.3/-2.0	-9.5/-13.0

Generally, results for all frontal passages, including those which did not lead to cold pools, were fairly similar to that for only fronts that led to cold pools. The magnitude of all of the variable changes increased on average for fronts with cold pools rather than fronts without cold pools if all fronts are considered. However, the magnitude of all of the variable changes decreased on average for strong fronts with cold pools compared to strong fronts without cold pools.

Temperature shows lower average temperature falls in spring and higher temperature falls in winter than average. Pressure changes have a distinct minimum in magnitude in summer while during the winter pressure changes are largest on average. Water vapor mixing ratio decreases a much smaller amount in summer compared to the other three seasons. Moist static energy has the smallest average decrease in summer and largest average decrease in winter. Since moist static energy is a function of temperature and water vapor mixing ratio, these results reveal those dependencies in summer differences are much lower than the other seasons (a q_v influence), and winter differences are much higher than the other seasons (a T influence).

Correlations between the four variable changes were calculated for all fronts (Table 6.3) and fronts that yielded cold pools (Table 6.4). Summer correlations are lower for all combinations involving temperature while winter correlations involving temperature are higher. ΔP correlations with Δq_v and Δhcp^{-1} were lowest in summer and winter. The correlation between Δq_v and $\Delta h/cp^{-1}$ is roughly the same all year. Notably, the correlation between ΔT and Δq_v is slightly negative in summer while it is positive for all other seasons. Also, the strong front correlations between ΔP and Δq_v are positive in the winter while it is negative for the other seasons. Correlations between Δq_v and Δhcp^{-1} were higher than correlations between ΔT and Δhcp^{-1} , suggesting that Δq_v has a stronger influence on Δhcp^{-1} than ΔT .

Differences are minimal between the correlations for frontal passages and only frontal passages that yield cold pools. Surprisingly, temperature correlations for stronger frontal passages during the summer have lower values than temperature correlations involving all frontal passages. These correlations suggest that stronger fronts have more varied structure than weaker fronts, possibly a result of the greater likelihood of convective rather than stratiform precipitation events in the summer.

6.2 Convergence/Divergence

It is expected that ahead of a frontal passage convergence would be likely to occur while behind a frontal passage divergence would be likely to occur. Cold pools are marked by the presence of significant divergence associated with a frontal passage, generally a short time after frontal passage occurs. As noted earlier, the divergence values were averaged over 15 minutes to smooth out some timing discrepancies that may occur in a study with large station spacing.

The divergence values were calculated at the beginning, middle, and end of each triangles' frontal passage. The beginning of a frontal passage is defined as the timestep where the first of the three triangle corner points reaches a local maximum front score. The end of a frontal passage is the timestep where the third of the three triangle corner points reaches a local maximum front score. The middle of the frontal passage is the halfway point between the first and last timestep. If there are an even number of timesteps then the two middle divergence values are averaged.

Table 6.3 – Correlations between ΔT , ΔP , Δq_v , and Δhcp^{-1} for all frontal passages (FS3+ / FS5+).

Season	$\Delta T, \Delta P$	$\Delta T, \Delta q_v$	$\Delta T, \Delta hcp^{-1}$	$\Delta P, \Delta q_v$	$\Delta P, \Delta hcp^{-1}$	$\Delta q_v, \Delta hcp^{-1}$
Spring (MAM)	-0.32/-0.44	0.36/0.31	0.61/0.61	-0.20/-0.15	-0.24/-0.28	0.94/0.94
Summer (JJA)	-0.15/-0.06	-0.01/-0.11	0.33/0.19	-0.13/-0.14	-0.17/-0.15	0.92/0.95
Fall (SON)	-0.23/-0.17	0.42/0.41	0.65/0.65	-0.32/-0.22	-0.33/-0.24	0.95/0.96
Winter (DJF)	-0.41/-0.38	0.54/0.47	0.80/0.77	-0.14/+0.17	-0.28/-0.03	0.92/0.93
Annual	-0.28/-0.32	0.28/0.22	0.58/0.53	-0.20/-0.17	-0.25/-0.25	0.93/0.94

Table 6.4 – Correlations between ΔT , ΔP , Δq_v , and Δhcp^{-1} for frontal passages which yield cold pools (FS3+ / FS5+).

Season	$\Delta T, \Delta P$	$\Delta T, \Delta q_v$	$\Delta T, \Delta hcp^{-1}$	$\Delta P, \Delta q_v$	$\Delta P, \Delta hcp^{-1}$	$\Delta q_v, \Delta hcp^{-1}$
Spring (MAM)	-0.32/-0.46	0.38/0.31	0.65/0.61	-0.19/-0.18	-0.27/-0.31	0.95/0.94
Summer (JJA)	-0.13/-0.04	-0.02/-0.12	0.33/0.19	-0.12/-0.13	-0.18/-0.15	0.93/0.95
Fall (SON)	-0.22/-0.18	0.40/0.41	0.67/0.65	-0.29/-0.25	-0.34/-0.28	0.95/0.96
Winter (DJF)	-0.44/-0.43	0.55/0.46	0.83/0.77	-0.07/+0.15	-0.26/-0.08	0.92/0.92
Annual	-0.27/-0.32	0.25/0.19	0.57/0.51	-0.20/-0.19	-0.26/-0.28	0.93/0.94

The divergence values for all frontal passages were calculated and shown in Table 6.5. On average, the triangles did have strong convergence ($div. < -10^{-4} \text{ s}^{-1}$) as the front initially reaches the triangle. The magnitude of convergence had small differences between seasons, with the convergence for all fronts being slightly weaker in winter and the convergence for strong fronts being stronger in fall and spring than summer and winter. For fronts at the middle of a triangle, there was a large seasonal difference. Summer frontal passages had divergence on average at the middle of a frontal passage while the other three seasons still maintained convergence. At the end of a frontal passage summer had the strongest divergences on average while winter had the weakest divergence. End of front divergence for summer was roughly the same as the beginning of front convergence. For the other three seasons the magnitude of convergence at the beginning of a frontal passage was much larger than the magnitude of divergence at the end of a frontal passage.

Divergence values for only the frontal passages which yielded cold pools are shown in Table 6.6. Since cold pools require the divergence threshold to be exceeded, the end divergence and middle divergence values are much higher than for all frontal passages data. The seasonal pattern remains; however, as summer has the highest divergence in the middle and end of frontal passages while winter has the lowest divergence for the end of frontal passages. Notable is the fact that the beginning divergence values show roughly the same convergence as for all frontal passages with only a very slight reduction. This suggests that divergence behind a front is not significantly dependent on convergence ahead of a front.

6.3 Seasonal Distribution

The seasonal distribution of frontal passages and cold pools was determined. For this calculation, instead of the stations of each triangle that experienced a front or cold pool being summed, it is the number of triangles that experienced a front or cold pool that is summed (Table 6.7). There were more frontal passages and cold pools during the summer than the other seasons. Winter had the fewest number of frontal passages and cold pools. Seasonal variation between convective and stratiform precipitation is likely the primary influence in this result. Frontal passages during

Table 6.5 – Divergence values at the beginning, middle, and end of all triangle frontal passages experienced by Mesonet triangles from 1997-2011 by season (FS3+ / FS5+) in s^{-1} .

Season	Beg. Div.	Mid. Div.	End. Div.
Spring (MAM)	$-1.40E^{-4}/-2.00E^{-4}$	$-1.55E^{-5}/-2.55E^{-5}$	$6.50E^{-5}/8.08E^{-5}$
Summer (JJA)	$-1.32E^{-4}/-1.72E^{-4}$	$1.87E^{-5}/2.47E^{-5}$	$1.24E^{-4}/1.61E^{-4}$
Fall (SON)	$-1.37E^{-4}/-2.02E^{-4}$	$-3.12E^{-5}/-5.30E^{-5}$	$5.75E^{-5}/8.03E^{-5}$
Winter (DJF)	$-1.09E^{-4}/-1.75E^{-4}$	$-3.52E^{-5}/-6.36E^{-5}$	$2.30E^{-5}/2.94E^{-5}$
Annual	$-1.32E^{-4}/-1.87E^{-4}$	$-1.10E^{-5}/-1.83E^{-5}$	$7.50E^{-5}/1.01E^{-4}$

Table 6.6 – Divergence values at the beginning, middle, and end of triangle frontal passages yielding cold pools experienced by Mesonet triangles from 1997-2011 by season (FS3+ / FS5+) in s^{-1} .

Season	Beg. Div.	Mid. Div.	End. Div.
Spring (MAM)	$-1.35E^{-4}/-1.86E^{-4}$	$3.47E^{-5}/2.77E^{-5}$	$1.26E^{-4}/1.36E^{-4}$
Summer (JJA)	$-1.29E^{-4}/-1.70E^{-4}$	$4.69E^{-5}/4.63E^{-5}$	$1.62E^{-4}/1.89E^{-4}$
Fall (SON)	$-1.35E^{-4}/-1.98E^{-4}$	$2.11E^{-5}/1.90E^{-6}$	$1.27E^{-4}/1.45E^{-4}$
Winter (DJF)	$-9.82E^{-5}/-1.62E^{-4}$	$2.51E^{-5}/4.22E^{-5}$	$9.58E^{-5}/9.66E^{-5}$
Annual	$-1.29E^{-4}/-1.78E^{-4}$	$3.68E^{-5}/3.02E^{-5}$	$1.38E^{-4}/1.58E^{-4}$

the summer also had the highest rates of yielding cold pools. Stronger fronts resulted in higher odds of cold pool formation which is expected since a stronger front would tend to have higher divergence on average.

6.4 Diurnal Distribution

Also calculated was the diurnal distribution of frontal passages and cold pools. Since data is collected every 5 minutes, the number of fronts at all triangles were added up over hourly periods (0000-0055 UTC, 0100-0155 UTC, ..., 2300-2355 UTC). Seasons were defined as: MAM for spring, JJA for summer, SON for fall, and DJF for winter.

There is a significant seasonal difference in the diurnal distribution of frontal passages (Figure 6.1). In the summer (Fig. 6.1b) there is a large spike in frontal passage frequency in the afternoon from 20-1 UTC with frontal passage frequencies twice as high as the rest of the day. The other three seasons have much smaller variation in

Table 6.7 – Number of frontal passages and cold pools experienced by Mesonet triangles from 1997-2011 by season (FS3+ / FS5+).

Season	# Fronts	# Cold Pools	% Fronts w/ Cold Pools
Spring (MAM)	23,811/8,329	13,820/5,397	58%/65%
Summer (JJA)	22,785/9,014	18,083/7,855	79%/87%
Fall (SON)	13,009/4,442	6,645/2,620	51%/59%
Winter (DJF)	12,539/3,843	4,329/1,530	35%/40%
Annual	72,144/25,628	42,877/17,402	59%/68%

the diurnal cycle. Presumably, more years would make for more smoothing of the data.

The standard deviations are rather large, a result that comes from the tendency for frontal passages to largely appear at the same time for a given system moving through Oklahoma since a single synoptic front can sweep through most of the counties in a few hours. Despite it being impossible for there to be more strong frontal passages than total fronts, the standard deviations of 3+ fronts and 5+ fronts do overlap some which means it can be expected that some years have more strong fronts in an hour than other years would have total fronts in that hour. Likewise, it is expected that there are years where total frontal passages are less common than strong frontal passages are for a given hour in a different year. Notably, the standard deviation for strong frontal passages extends below 0 which is impossible and a result of a low average with large outliers on the high side yielding a large standard deviation.

The diurnal distribution of cold pools is very similar to that for frontal passages (Fig. 6.2). One slight difference is that the winter has almost no diurnal cycle in cold pool frequency. The difference between the highest and lowest average frequency hour for spring, summer, and fall, are all over 50%. Summer's maximum difference is over 200% higher in the most frequent hour compared to the least frequent hour.

The percentage of frontal passages yielding cold pools was also calculated (Fig. 6.3). For most hours of the day in each of the 4 seasons the percentage of strong fronts resulting in cold pools was higher than the percentage of all fronts resulting in cold pools. Consistently throughout the year, it was the evening hours that had the largest spread between all and strong frontal passages leading to cold pools.

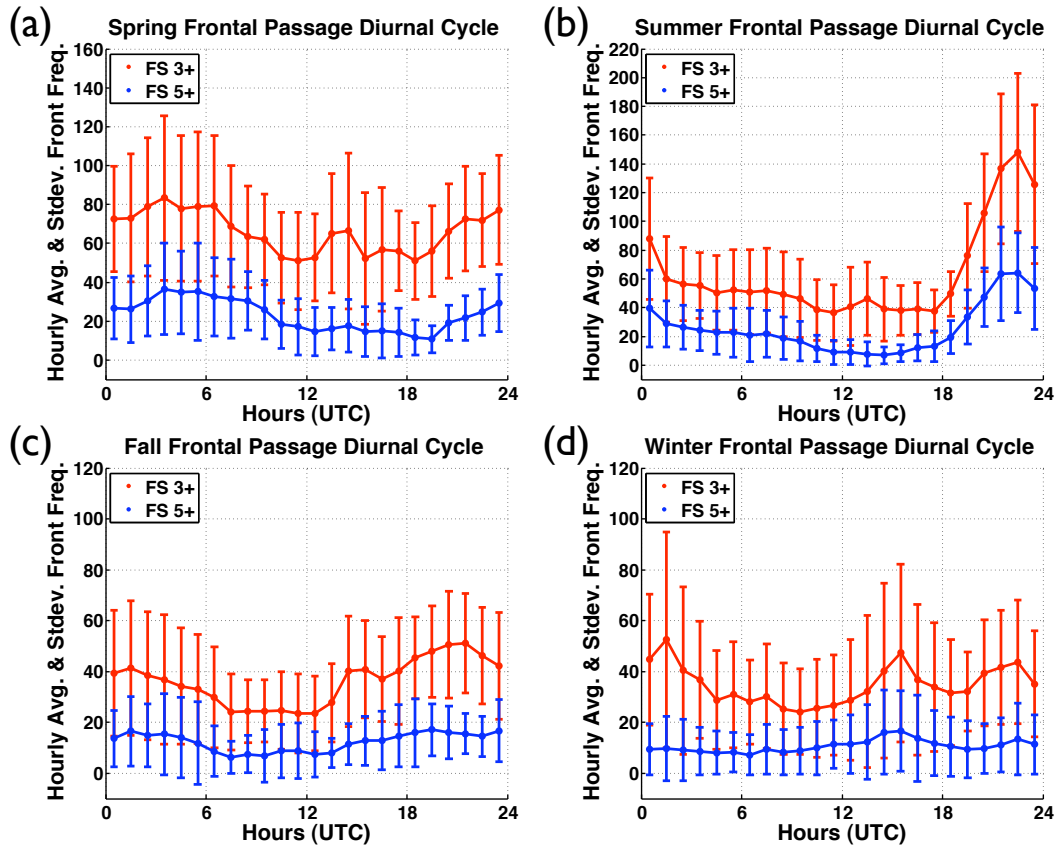


Figure 6.1 – Seasonally averaged diurnal cycle (in UTC time) of all frontal passages at triangles in the Oklahoma Mesonet from the 1997-2011 period along with standard deviations. Results are shown for (a) spring, (b) summer, (c) fall, and (d) winter and for all frontal passages (red) and strong frontal passages (blue).

In the spring (Fig. 6.3a) roughly 60% of fronts resulted in cold pools throughout most of the day. The morning hours were the exception with the percentage dropping below 50% for several hours (15-19 UTC). The summer (Fig. 6.3b) had the highest rate of frontal passages yielding cold pools, exceeding 90% in the evening hours for strong frontal passages. There is a much slighter drop in the percentage of frontal passages yielding cold pools in the morning hours for the summer than there was in the spring, and this drop did not occur for strong frontal passages. No individual hour falls below 70% of total fronts yielding cold pools. In the fall evening hours (Fig. 6.3c) 60% of frontal passages and 75% of strong frontal passages resulted in cold pools. During the day these percentages fell to between 40 and 55% until the

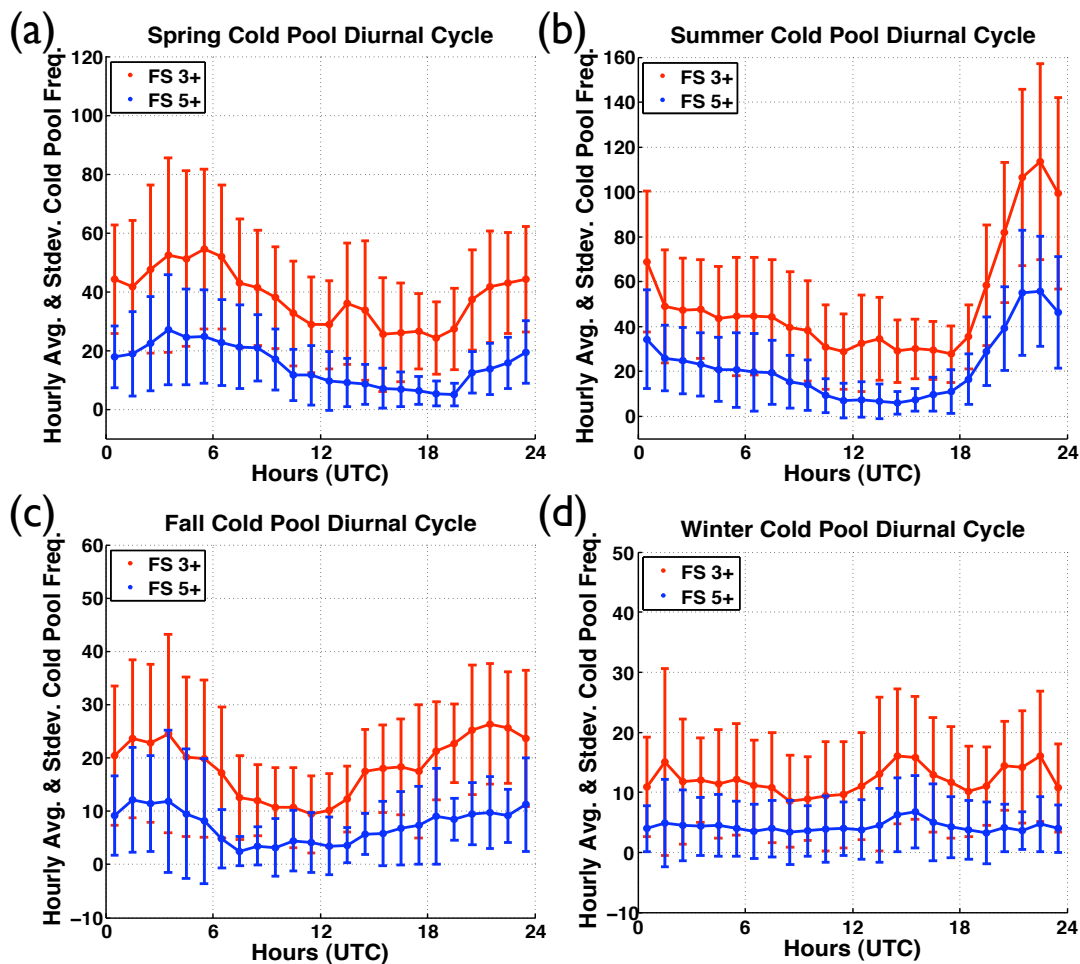


Figure 6.2 – Seasonally averaged diurnal cycle (in UTC time) of all cold pools at triangles in the Oklahoma Mesonet from the 1997-2011 period along with standard deviations. Results are shown for (a) spring, (b) summer, (c), fall, and (d) winter and for all frontal passages which yielded cold pools (red) and strong frontal passages which yielded cold pools (blue).

mid-afternoon. In the winter (Fig. 6.3d) the rate of frontal passages resulting in cold pools is consistent throughout the day between 30 and 40%.

6.5 Geographic Distribution

Finally, the geographic distribution of frontal passages and cold pools across the Mesonet was computed. An issue that became apparent was the dependence of frontal passage frequency on the area and maximum side length of the triangle. For this reason, triangles with side lengths $> 80\text{km}$, which were located primarily along the

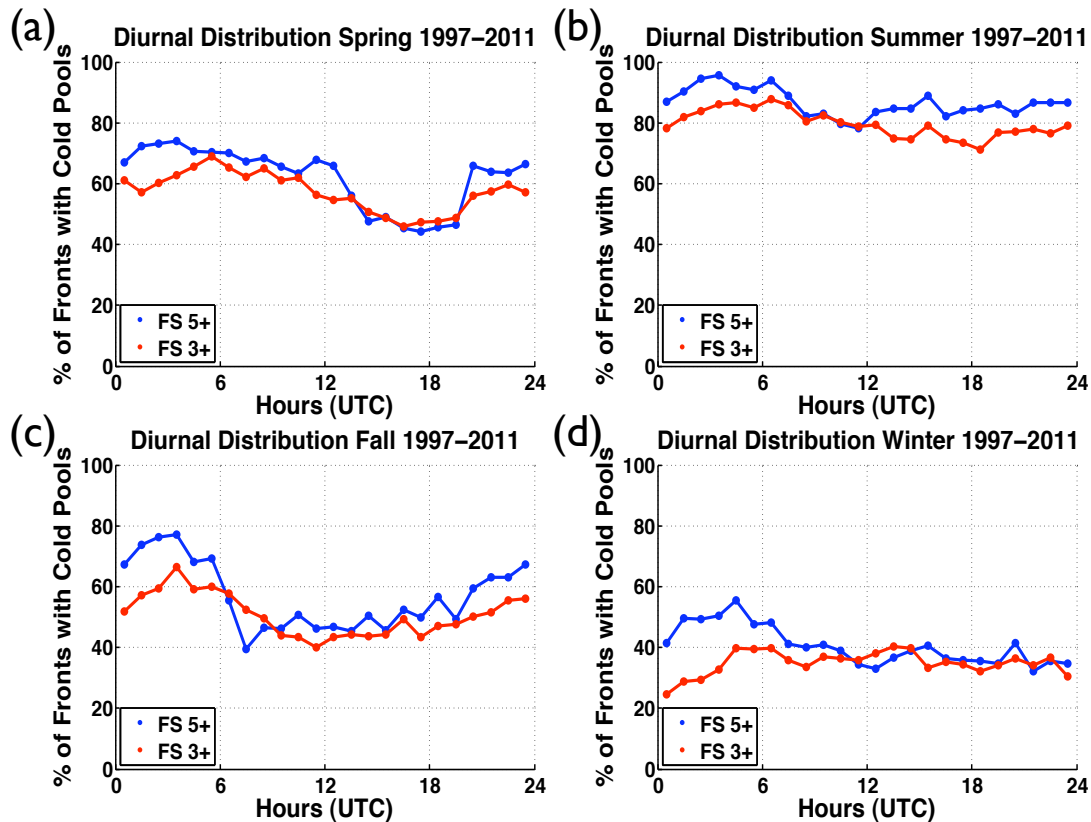


Figure 6.3 – Seasonally averaged diurnal cycle (in UTC time) of the percentage of all (red) and strong (blue) fronts that yield cold pools. Results are shown for (a) spring, (b) summer, (c), fall, and (d) winter.

outer boundary, were dropped from the Delaunay triangulation grid and are not used in any of the results detailed throughout this work. As a result, 10-13 stations a year removed due to the side length issue from the 99-104 original stations that met the observation threshold. Linear regressions of the remaining triangles were performed using a least-squares fit to determine the dependence on triangle area (Fig. 6.4) and maximum side length (Fig. 6.5).

Smaller triangles and triangles with shorter maximum side lengths had lower frequencies of frontal passages and cold pool occurrence on average. This was expected since all three triangle corners had to be activated to trigger a frontal passage. With small, isolated thunderstorm events this is less likely to be captured on portions of the grid with lower resolution, as well as very slow moving storms that failed to reach all

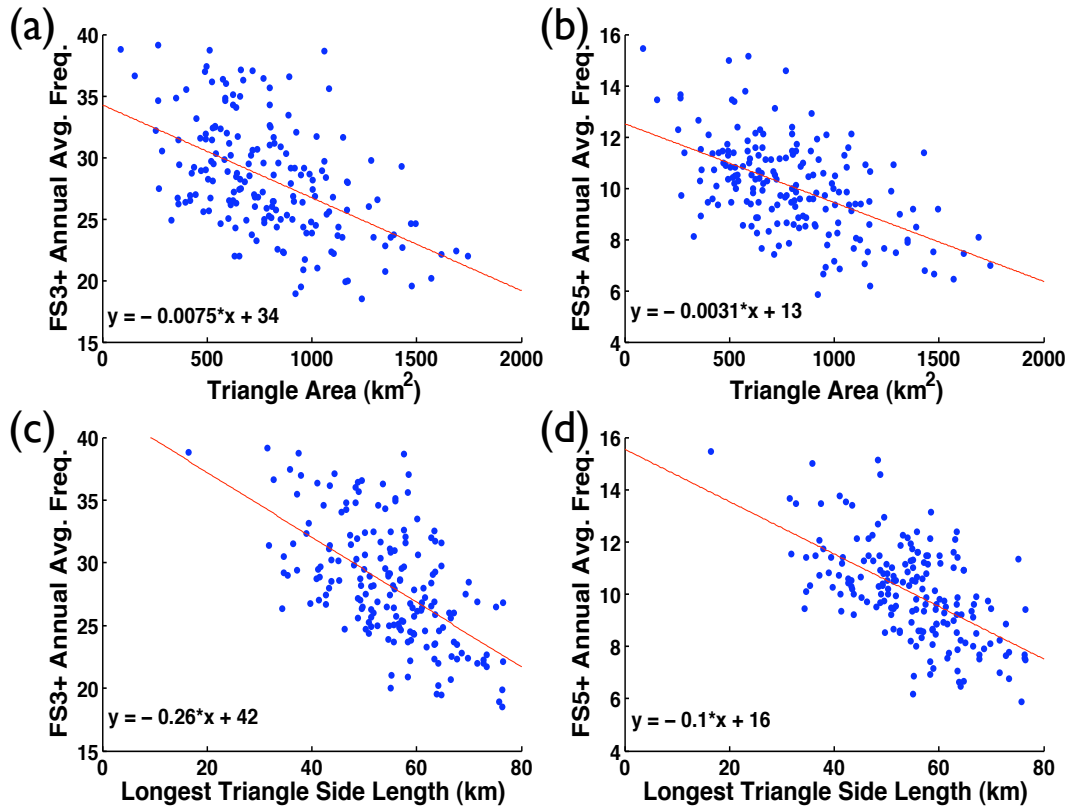


Figure 6.4 – Scatterplots with linear regression lines for (a) annually averaged frontal passage frequency and Mesonet triangle area, (b) annually averaged strong frontal passage frequency and Mesonet triangle area, (c) annually averaged frontal passage frequency and longest Mesonet triangle side length, and (d) annually averaged strong frontal passage frequency and longest Mesonet triangle side length.

three corners within two hours. The following equations (Eq. 6.1-6.8) are the results of the linear fits for fronts and cold pools:

$$Fronts_{FS3+} = -7.5E^{-3} \times TriangleArea + 34 \quad (6.1)$$

$$Fronts_{FS5+} = -3.1E^{-3} \times TriangleArea + 13 \quad (6.2)$$

$$Fronts_{FS3+} = -0.26 \times TriangleMaxSideLength + 42 \quad (6.3)$$

$$Fronts_{FS5+} = -0.10 \times TriangleMaxSideLength + 16 \quad (6.4)$$

$$ColdPools_{FS3+} = -1.1E^{-2} \times TriangleArea + 25 \quad (6.5)$$

$$ColdPools_{FS5+} = -3.9E^{-3} \times TriangleArea + 10 \quad (6.6)$$

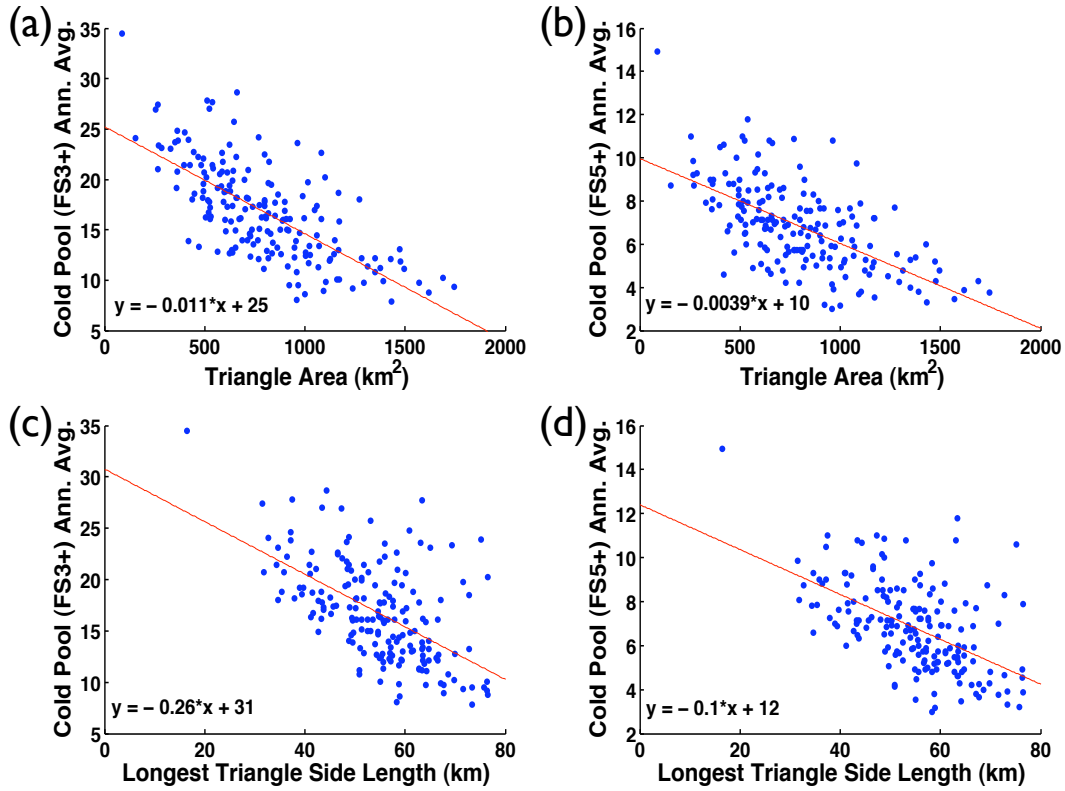


Figure 6.5 – Scatterplots with linear regression lines for (a) annually averaged cold pool frequency and Mesonet triangle area, (b) annually averaged strong cold pool frequency and Mesonet triangle area, (c) annually averaged cold pool frequency and longest Mesonet triangle side length, and (d) annually averaged strong cold pool frequency and longest Mesonet triangle side length.

$$ColdPools_{FS3+} = -0.26 \times TriangleMaxSideLength + 31 \quad (6.7)$$

$$ColdPools_{FS5+} = -0.10 \times TriangleMaxSideLength + 12 \quad (6.8)$$

Each triangle was adjusted using these regression lines by assuming all triangles had the average area and side length and moving the scatterplot point value along a line with the same slope as the regression line. The end result of this adjustment is the geographic distributions of fronts (Fig. 6.6) and cold pools (Fig. 6.7) displayed. Points on these plots are station centroids for triangles that were present in the Mesonet for over 5 years with the size of the point scaled by the number of years that the point is a centroid (max: 15). Since some stations are either removed from the Mesonet, fail to meet the observation threshold for a year, or are moved to a different location, the triangles are not constant. The grid applies to the 1997 data; points

that are not centroids of these triangles are centroids for triangles that are present later in the dataset.

For frontal passages adjusted by area (Fig. 6.6a) a clear west to east gradient is apparent with western regions of Oklahoma having larger frequencies of frontal passages than eastern regions of Oklahoma. Skinny triangles along the borders (ones that remained in the grid) appear to still underestimate the number of frontal passages that occur, even after the area adjustment. The triangle with the highest frequency of frontal passages before the adjustment is the small triangle in the north central part of the state. After the adjustment this triangle has a lower frequency than the stations to its west. Strong fronts adjusted by area (Fig. 6.6b) show a similar distribution with only minor differences. The southwestern corner appears to have a lower frequency of strong fronts relative to its value for total fronts. Also, the stations in the north central region have the highest rates of strong fronts.

For frontal passages adjusted by maximum side length (Fig. 6.6c) the same west to east pattern remains. The main difference between the area adjustment and the length adjustment is that for skinny triangles the length adjustment yields a much higher frequency value than the area adjustment. Additionally, more equilateral triangles have a lower frequency value with the length adjustment than the area adjustment. This is the case for all frontal passages and for the strong frontal passages (Fig 6.6d).

For cold pools adjusted for area the west to east gradient is much weaker than it is for frontal passages (Fig. 6.7a). West-central Oklahoma appears to have a narrow filament of higher than average frequencies of cold pool occurrence while the northwest and southwest have lower rates of cold pools compared to state average than they have frontal passages. Cold pools from strong fronts (Fig. 6.7b) show roughly the same pattern. Cold pools adjusted for length instead of area (Fig. 6.7c, 6.7d) show the same differences compared to area as was the case for frontal passages. The border edge skinny triangles have the highest rates of cold pools after the adjustment. It would appear at a glance that area is the more accurate adjustment of the two when it comes to cold pools.

The distribution of the difference between means for each station relative to the Mesonet average was calculated for stations that were present more than 5 of the

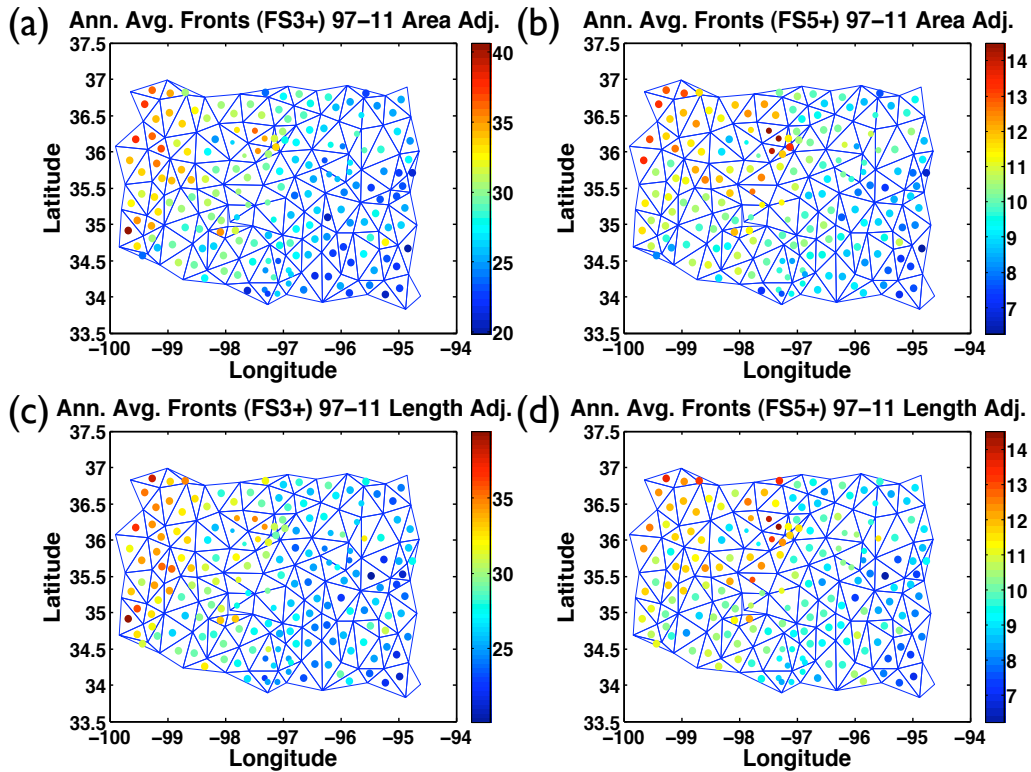


Figure 6.6 – Geographic distribution of (a) all frontal passages, adjusted for triangle area, (b) strong frontal passages, adjusted for triangle area, (c) all frontal passages, adjusted for maximum triangle side length, and (d) strong frontal passages, adjusted for maximum triangle side length. Size of dots represents the number of years the triangle centroid was at that location (1997-2011). Only triangles that were present more than 5 years are shown. The grid is the 1997 triangles; since the grid can change each year the 1997 grid is only a close representation.

15 years. The Mesonet average compared to a station would only include the years in which that station was part of the Mesonet average. The Student t -scores were calculated for 4 sets of data: 1) the original grid, 2) an adjusted grid that removed triangles with maximum triangle side length > 80 km, 3) the adjusted grid with the frequencies adjusted for triangle area, and 4) the adjusted grid with the frequencies adjusted for maximum triangle side length with the average t -score magnitude shown (Table 6.8). For sample sizes of 6-15 years, t -scores > 2.447 (for 6 years) and > 2.131 for 15 years are different than the Mesonet average at the 95% confidence level.

For the unadjusted grid, frontal passages average 2.18 and 1.61 for all fronts

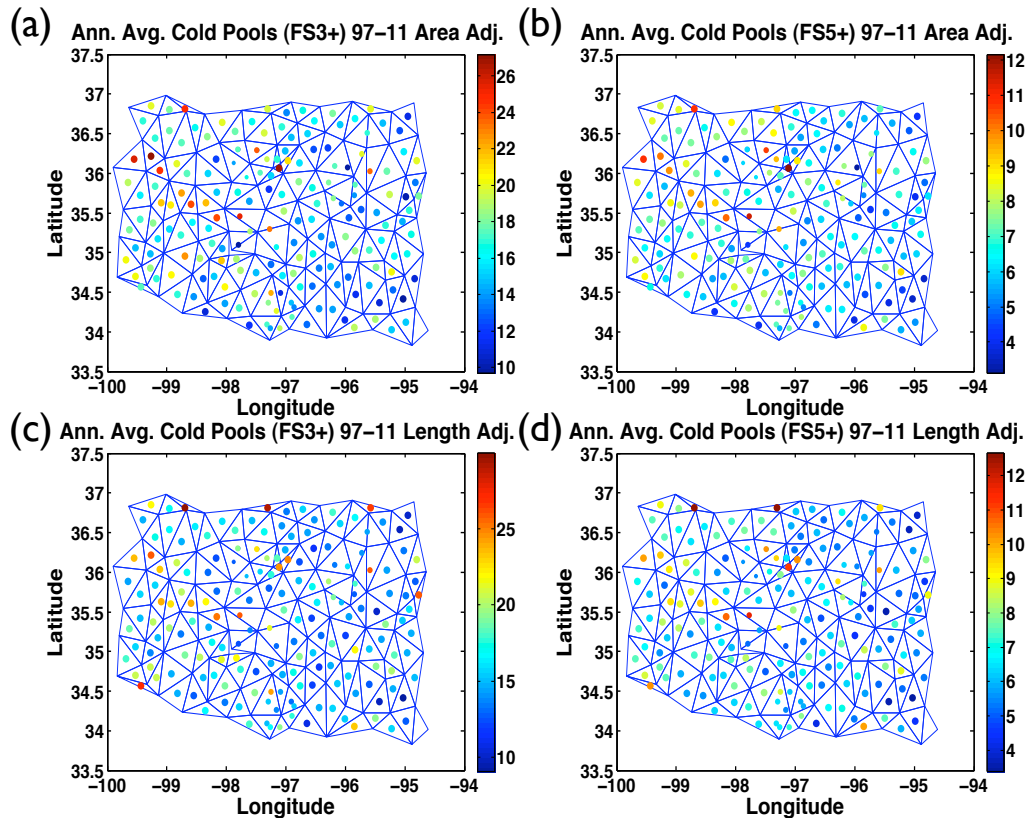


Figure 6.7 – Geographic distribution of (a) all fronts which yield cold pools, adjusted for triangle area, (b) strong fronts which yield cold pools, adjusted for triangle area, (c) all fronts which yield cold pools, adjusted for maximum triangle side length, and (d) strong fronts which yield cold pools, adjusted for maximum triangle side length. Size of dots represents the number of years the triangle centroid was at that location (1997-2011). Only triangles that were present more than 5 years are shown. The grid is the 1997 triangles; since the grid can change each year the 1997 grid is only a close representation.

and strong fronts respectively. The average t-score is much higher for cold pools, at 3.36 and 2.26 for all cold pools and cold pools associated with strong fronts. When the extra-long triangles above 80 km in side length are removed the t-scores decrease in magnitude roughly 10% for fronts and a smaller decrease for cold pools. The adjustments for area and length significantly reduced the magnitude of the t-scores. This shows that both area and side length play a role in causing triangles to overestimate or underestimate the frequency of frontal passages. For all grids and adjustments the strong fronts and cold pools for strong fronts had lower t-scores than

Table 6.8 – Average magnitude of Student t -scores from distribution of difference between mean scores for triangles that were present in the Mesonet for over 5 years. Values are given for fronts and cold pools of both strengths. The Original column contains the t -scores for the original grid. The Grid column refers to t -scores for the grid adjusted to remove triangles with too-large side lengths. The final two columns have the t -scores with the grid adjustment and the area and triangle side length adjustments, respectively.

Adjustments	Original	Grid	Grid & Area	Grid & Length
Fronts (FS3+)	2.18	1.90	1.58	1.47
Fronts (FS5+)	1.61	1.37	1.10	1.06
Cold Pools (FS3+)	3.36	3.27	2.21	2.62
Cold Pools (FS5+)	2.26	2.13	1.60	1.74

for all fronts and cold pools. The average magnitude of the t -score for frontal passages was lower with the length adjustment than with the area adjustment. However, the average magnitude of the t -score for cold pools was lower with the area adjustment than with the length adjustment. Also, frontal passages had lower average t -scores than cold pools for all grids and adjustments.

CHAPTER 7

DISCUSSION

The results detailed in the preceding chapters extend analysis of Oklahoma Mesonet data to a 15-year dataset, providing a much larger sample size for seasonal analyses of frontal passages and convective cold pools. This allows for clearer signals to appear in the data with increased certainty that the results obtained here are representative.

7.1 Research Findings

There was a maximum correlation between updrafts and downdrafts with precipitation during the summer months with a minimum correlation in winter (Table 4.1). Convective precipitation from cumulonimbus clouds is more prevalent in the summer as a result of daytime convective heating leading to the generation of late afternoon and evening thunderstorms and squall lines. This increase in convective precipitation is evident by the increased frequency of frontal passages and cold pools in the diurnal pattern during the summer months (Fig. 6.1-6.2). Additionally, there is more moisture in the atmosphere during the summer which can lead to heavier precipitating storms. As a result, strong updrafts and downdrafts feature more prominently alongside the summertime convection which leads to a more distinct and correlated updraft-downdraft couplet. In the winter, due to the colder temperatures, moisture levels are much lower. Updrafts and downdrafts that tend to be weaker lead to a larger proportion of precipitation that is stratiform. The weaker updrafts and downdrafts result in a less prominent couplet and reduced correlation.

However, other correlations decreased during the summer relative to the other seasons, such as most of the correlations between ΔT , ΔP , Δq_v , and Δh_{cp}^{-1} (Tables 6.1 and 6.2). The correlation between ΔT and Δq_v was even slightly negative for the summer when it was positive for the other seasons. The correlation of ΔT with ΔP

was near 0 during the summer with -0.04 for strong summer fronts that led to cold pools. This suggests that the vertical structure of the temperature perturbation in the cold pools varies significantly from case to case. The variations in structure are expected to be larger in convective systems rather than in stratiform precipitation systems due to deeper and more varied updraft, boundary layer, and cold pool heights. Three-dimensional data would aid in resolving the vertical features in the Mesonet. For this reason, case studies involving intense observations periods (IOPs) are the most productive to pursue in future research. The MC3E period is one such IOP that would have an enhanced capacity to resolve 3D structure for cases.

Frontal passages and cold pools generally had similar statistics for changes between variables and correlations. However, Δq_v and Δhcp^{-1} had slightly larger values for cold pools (roughly 10%) than for all frontal passages though the seasonal pattern remained the same. This is likely a result of the tendency of dry frontal passages to not have cold pools due to a lack of strong divergence behind those fronts. The lack of precipitation in dry frontal passages would reduce the magnitude of the ensuing q_v fall which in turn reduces the magnitude of the hcp^{-1} decrease.

7.2 Comparisons to Previous Studies

Some of the statistics that gained a much larger sample size relative to previous work were the correlations between updrafts and downdrafts with precipitation. Sun and Krueger (2012) in their Figure 5 showed correlations that peaked slightly higher for MJJA 1997 than for the JJA period for the 15 years of Mesonet data. Their peak correlations were roughly 0.6 for M_u with precipitation and M_d with precipitation, 0.65 for M_u^+ with precipitation, and 0.7 for M_d^+ with precipitation whereas the JJA period in the 15-year dataset had correlations of 0.48, 0.55, and 0.59, respectively. Also, their M_d and M_d^+ values lagged precipitation and the updrafts by an hour. However, the 1997-2011 analysis in this study used 3-hour averaging which would likely smooth out the expected maximum correlations making the results roughly the same between the 15-year dataset and the Sun and Krueger analysis as would be expected.

Studies have observed pressure and temperature changes in cold pool cases. In

one such study (Engerer et al., 2008) the average pressure rise in cold pools from 39 MCS events between April and August was 4.5 mb while the average temperature fall was 9.5 K. It is safe to assume that these MCS events were chosen because they were particularly strong so the comparison for the 15-year dataset would be strong fronts which averaged a 3.6-mb pressure rises in spring, a 2.5-mb pressure rises in summer, and a 7.7-K temperature drops in both spring and summer. Though the Engerer et al. study found larger pressure and temperature changes on average, considering the that 15-year dataset was diurnally adjusted, and the much larger sample size for 15-year dataset of strong fronts that may be weighted down with weaker, albeit still strong, fronts, the results are in reasonable agreement.

The geographical distribution of frontal passages suggests a west to east gradient with a higher frequency of frontal passages on the westward side of Oklahoma. One likely influence is the dryline which frequently develops in the lee of the Rocky Mountains and advances into Oklahoma where numerous case studies have been made over the years (McCarthy and Koch, 1982; Ziegler and Hane, 1993; Buban et al., 2007). A climatology of springtime dryline position matches well with the frontal passage geographic distribution anomaly pattern (Hoch and Markowski, 2005). Their Fig. 2 showed that the dryline most frequently was located around 101W longitude and the dryline location range is generally from 103W to 97E near Oklahoma City with rare occurrences farther eastward. The west to east pattern is weaker when it comes to cold pools, suggesting that western stations have a higher rate of frontal passages not resulting in cold pools.

CHAPTER 8

CONCLUSIONS

8.1 Summary of Results

A 15-year climatology of Oklahoma Mesonet frontal passages and cold pools was created and analyzed. Previous studies involving cold pools in the Oklahoma Mesonet have only looked at shorter time periods, with a focus on other features such as MCSs (Engerer et al., 2008) and squall lines (Adams-Selin and Johnson, 2010).

Surface divergence statistics related to near-cloud-base convective mass flux were calculated. The strongest convergence and divergence, on average, were during the spring, while the weakest were during the winter. The annual pattern was fairly consistent from year to year. Correlations were calculated between convergence, divergence, and precipitation which resulted in higher correlations in the summer and lower correlations in the winter. Strong convergence and divergence had higher correlations with each other and precipitation than all convergence and divergence had with each other and precipitation. Wet spring and summer days had the strongest convergence and divergence while dry summer and fall days had the weakest convergence and divergence.

Frontal passages and cold pools were examined in detail for several case studies, of which four were outlined here: 1) 13 June 1997, 2) 15-16 June 2002, 3) 20 May 2011 and 4) 24-25 May 2011. These fronts were captured quite well as they progressed through the Oklahoma Mesonet. Even some finer details were picked up on like weaknesses in the line, represented by lower front scores and weaker convergence-divergence gradients across the front. The effects of convective storm type were distinct in the 24-25 May 2011 case during the tornado outbreak as the convergence-divergence gradient was minimal in many areas and times in the particular case. Cold pool extents and longevity varied from case to case.

Frontal passages, with or without cold pools, had smaller magnitudes of ΔP , Δq_v , and Δhcp^{-1} during the summer season frontal passages than the other seasons. Spring had the smallest magnitude of ΔT . Winter had the largest magnitudes, with the exception of Δq_v , which was slightly larger in spring and fall. Correlations involving ΔT were lowest in the summer and highest during the winter except for strong spring ΔT correlations with ΔP . Correlations with ΔP and Δq_v or Δhcp^{-1} were lowest in the summer and winter. The correlation between Δq_v or Δhcp^{-1} was above 0.9 year-round. Of particular note is the anomalously negative correlation between ΔT and Δq_v during the summer and the positive correlation between ΔP and Δq_v for strong winter frontal passages. The changes in the variables and their correlations were generally similar for cold pool producing fronts as they were for all fronts.

Seasonally, summer has the highest frequency of frontal passages and cold pools with spring second. Summer has the highest percentage of frontal passages that lead to cold pools. Winter was lowest in all of these categories. The diurnal cycle of fronts and cold pools has a strong seasonal variation. During the summer, frontal passages and cold pools are most frequent in the late afternoon to evening hours, coinciding with daytime-heating-induced convection. The other seasons have much smaller variation in frontal passage and cold pool frequency in the diurnal cycle. The summer pattern is the dominant influence on the annual pattern for the diurnal cycle.

Geographically, the size of Mesonet triangles, in terms of area and maximum side length, has a large influence on the analyzed frequency of frontal passages and cold fronts. After this analysis artifact is accounted for, western regions of Oklahoma experienced higher frequencies of frontal passages in particular, and cold pools to a lesser degree, than eastern regions. Frontal passages had lower differences between means Student t -score magnitudes from station to Mesonet average than cold pools. However, the area adjustment led to lower average t -score magnitudes for cold pools than the length adjustment, while the length adjustment led to lower average t -score magnitudes for frontal passes than the area adjustment.

8.2 Future Research Possibilities

This research could be expanded in the future by evaluating these methods with simulations using models such as WRF (Weather Research and Forecasting) and SAM (System for Atmospheric Modeling). Particularly useful would be the increased resolution in a model relative to the Oklahoma Mesonet. A higher resolution would improve representations, especially for cases of smaller scale features and isolated convection that can be missed on grids with 40-km resolution.

Additionally, the Mesonet observations resided in only two spatial dimensions, so obtaining three-dimensional data, whether observationally or with model output, will help better understand the reasons behind the low correlations between changes in variables during summer frontal passages. The MC3E field campaign produced an extensive set of data which can be used for case study analyses in three dimensions.

Another possibility is to incorporate more variables into the front and cold pool detection methods. Wind shifts mark frontal passages and could be included rather than just looking at divergence. Precipitation is necessary for evaporative cooling, though the precipitation does not have to reach the ground for evaporative cooling to occur. Potential temperature has been used previously in cold pool studies rather than temperature (Engerer et al., 2008).

Estimating rain evaporation from surface pressure anomalies in cloud-resolving model simulations could be used to develop a method that could be implemented in cold pool analysis. Fujita had developed methods to calculate rain evaporation which assumed that the entirety of the pressure rise was a result of evaporated precipitation (Fujita, 1959). Comparing Mesonet estimated rain evaporation to model results can better identify the method best suited for developing rain evaporation estimates using only surface observations.

Furthering the understanding of cold pools could lead to better representation of them in forecast models, as well as improved analysis of gust fronts, squall lines, MCSs, and other features associated with convection. Improved tracking of mesoscale and synoptic conditions, in turn, would lead to increased preparedness when it comes to severe weather events.

REFERENCES

- Adams-Selin, R. D. and R. H. Johnson, 2010: Mesoscale surface pressure and temperature features associated with bow echoes. *Mon. Wea. Rev.*, **138**, 212–227.
- Arakawa, A. and W. H. Schubert, 1974: Interaction of a cumulus cloud ensemble with large-scale environment, Part I. *J. Atmos. Sci.*, **31**, 674–701.
- Brock, F. V., K. C. Crawford, R. L. Elliott, G. W. Cuperus, S. J. Stadler, H. L. Johnson, and M. D. Eilts, 1995: The Oklahoma Mesonet: A technical overview. *J. Atmos. Oceanic. Technol.*, **12**, 5–19.
- Buban, M. S., C. L. Ziegler, E. N. Rasmussen, and Y. P. Richardson, 2007: The dryline on 22 May 2002 during IHOP: Ground-radar and in situ data analyses of the dryline and boundary layer evolution. *Mon. Wea. Rev.*, **135**, 2473–2505.
- Corfidi, S. F., 2003: Cold pools and MCS propagation: Forecasting the motion of downwind-developing MCSs. *Wea. Forecasting*, **18**, 997–1017.
- Crum, T. D., R. L. Alberty, and D. W. Burgess, 1993: Recording, archiving, and using WSR-88D data. *Bull. Amer. Meteor. Soc.*, **74**, 645–652.
- Crum, T. D., R. E. Saffle, and J. W. Wilson, 1998: An update on the NEXRAD program and future WSR-88D support to operations. *Wea. Forecasting*, **13**, 253–262.
- Davies-Jones, R., 1993: Useful formulas for computing divergence, vorticity, and their errors from three or more stations. *Mon. Wea. Rev.*, **121**, 1449–1458.
- Dawson II, D. T., M. Xue, J. A. Milbrandt, and M. K. Yau, 2010: Comparison of evaporation and cold pool development between single-moment and multimoment bulk microphysics schemes in idealized simulations of tornadic thunderstorms. *Mon. Wea. Rev.*, **138**, 1152–1171.
- Droegemeier, K. K. and R. B. Wilhelmson, 1985a: Three-dimensional numerical modeling of convection produced by interacting thunderstorm outflows. Part I: Control simulation and low-level moisture variations. *J. Atmos. Sci.*, **42**, 2381–2403.
- Droegemeier, K. K. and R. B. Wilhelmson, 1985b: Three-dimensional numerical modeling of convection produced by interacting thunderstorm outflows. Part II: Variations in vertical wind shear. *J. Atmos. Sci.*, **42**, 2404–2414.
- Droegemeier, K. K. and R. B. Wilhelmson, 1987: Numerical simulation of thunderstorm outflow dynamics. Part I: Outflow sensitivity experiments and turbulence dynamics. *J. Atmos. Sci.*, **44**, 1180–1210.

- Dubois, J. A. and P. L. Spencer, 2005: Computing divergence from a surface network: Comparison of the triangle and pentagon methods. *Wea. Forecasting*, **20**, 596–608.
- Engerer, N. A., D. J. Stensrud, and M. C. Coniglio, 2008: Surface characteristics of cold pools. *Mon. Wea. Rev.*, **136**, 4839–4849.
- Fujita, T., 1955: Results of detailed synoptic studies of squall lines. *Tellus*, **7**, 405–436.
- Fujita, T., 1959: Precipitation and cold air production in mesoscale thunderstorm systems. *J. Meteor.*, **16**, 454–466.
- Fulton, R. A., J. P. Breidenbach, D.-J. Seo, and D. A. Miller, 1998: The WSR-88D rainfall algorithm. *Wea. Forecasting*, **13**, 377–395.
- Grandpeix, J.-Y. and J.-P. Lafore, 2010: A density current parameterization coupled with Emanuel’s convection scheme. Part I: The models. *J. Atmos. Sci.*, **67**, 881–897.
- Grandpeix, J.-Y., J.-P. Lafore, and F. Cheruy, 2010: A density current parameterization coupled with Emanuel’s convection scheme. Part II: 1d simulations. *J. Atmos. Sci.*, **67**, 898–922.
- Grassotti, C., R. N. Hoffman, E. R. Vivoni, and D. Entekhabi, 2003: Multiple-timescale intercomparison of two radar products and rain gauge observations over the Arkansas-Red River Basin. *Wea. Forecasting*, **18**, 1207–1229.
- Hoch, J. and P. M. Markowski, 2005: A climatology of springtime dryline position in the U.S. Great Plains region. *J. Climate*, **18**, 2132–2137.
- Hohenegger, C. and C. S. Bretherton, 2011: Simulating deep convection with a shallow convection scheme. *Atmos. Chem. Phys.*, **11**, 10 389–10 406.
- James, R. P., P. M. Markowski, and J. M. Fritsch, 2006: Bow echo sensitivity to ambient moisture and cold pool strength. *Mon. Wea. Rev.*, **134**, 950–964.
- Johnson, R. H. and P. J. Hamilton, 1988: The relationship of surface pressure features to the precipitation and airflow structure of an intense midlatitude squall line. *Mon. Wea. Rev.*, **116**, 1444–1472.
- Loehrer, S. M. and R. H. Johnson, 1995: Surface pressure and precipitation life cycle characteristics of PRE-STORM mesoscale convective systems. *Mon. Wea. Rev.*, **123**, 600–621.
- McCarthy, J. and S. E. Koch, 1982: The evolution of an Oklahoma dryline. Part I: A meso- and subsynoptic-scale analysis. *J. Atmos. Sci.*, **39**, 225–236.
- McPherson, R. A., et al., 2007: Statewide monitoring of the mesoscale environment: A technical update on the Oklahoma Mesonet. *J. Atmos. Oceanic Technol.*, **24**, 301–321.
- Newton, C. W., 1950: Structure and mechanism of the prefrontal squall line. *J. Meteor.*, **7**, 210–222.

- Romero, R., C. A. Doswell III, and R. Riosalido, 2001: Observations and fine-grid simulations of a convective outbreak in northeastern Spain: Importance of diurnal forcing and convective cold pools. *Mon. Wea. Rev.*, **129**, 2157–2182.
- Rotunno, R., J. B. Klemp, and M. L. Weisman, 1988: A theory for strong, long-lived squall lines. *J. Atmos. Sci.*, **45**, 463–485.
- Stensrud, D. J., G. S. Manikin, E. Rogers, and K. E. Mitchell, 1999: Importance of cold pools to NCEP mesoscale Eta model forecasts. *Wea. Forecasting*, **14**, 650–670.
- Stoelinga, M. T., J. D. Locatelli, R. D. Schwartz, and P. V. Hobbs, 2003: Is a cold pool necessary for the maintenance of a squall line produced by a cold front aloft? *Mon. Wea. Rev.*, **131**, 95–115.
- Stumpf, G. J. and R. H. Johnson, 1991: The wake low in a midlatitude mesoscale convective system having complex convective organization. *Mon. Wea. Rev.*, **119**, 134–158.
- Sun, R. and S. K. Krueger, 2012: Mesoanalysis of the interactions of precipitating convection and the boundary layer. *J. Adv. Model. Earth Syst.*, **4**, M04004.
- Tepper, M., 1950: A proposed mechanism of squall lines: The pressure jump line. *J. Meteor.*, **7**, 21–29.
- Tompkins, A. M., 2001: Organization of tropical convection in low vertical wind shears: The role of cold pools. *J. Atmos. Sci.*, **58**, 1650–1672.
- Wakimoto, R. M., 1982: The life cycle of thunderstorm gust fronts as viewed with Doppler radar and rawinsonde data. *Mon. Wea. Rev.*, **110**, 1060–1082.
- Wallace, J. M. and P. V. Hobbs, 2006: *Atmospheric Science: An Introductory Survey*. 2nd ed. Academic Press., 483 pp.
- Weiss, C. C. and H. B. Bluestein, 2002: Airborne pseudo-dual doppler analysis of a dryline-outflow boundary intersection. *Mon. Wea. Rev.*, **130**, 1207–1226.
- Wilhelmson, R. B. and C.-S. Chen, 1982: A simulation of the development of successive cells along a cold outflow boundary. *J. Atmos. Sci.*, **39**, 1466–1483.
- Wilhelmson, R. B. and J. B. Klemp, 1978: A numerical study of storm splitting that leads to long-lived storms. *J. Atmos. Sci.*, **35**, 1974–1986.
- Ziegler, C. L. and C. E. Hane, 1993: An observational study of the dryline. *Mon. Wea. Rev.*, **121**, 1134–1151.